AIAA Aviation Forum and ASCEND co-located Conference Proceedings
29 July - 2 August 2024, Las Vegas, Nevada
AIAA AVIATION FORUM AND ASCEND 2024
10.2514/6.2024-3829

Modeling and Simulation of High Temperature Proton Exchange Membrane Fuel Cells in Parallel Hybrid Electric Turboprop Aircraft with Multi Whale Optimization Algorithms

Yi-Chih Wang* and Gokcin Cinar†
Department of Aerospace Engineering, University of Michigan, Ann Arbor, Michigan 48109

Integrating renewable energies, particularly hydrogen and fuel cells, into new sustainable aircraft configurations is essential to achieving the 2050 target of zero carbon emissions. This study presents a model for different power management controls of High-Temperature Proton Exchange Membrane Fuel Cells (HT-PEMFC) in a parallel hybrid electric turboprop aircraft (Dash 8 Q300), utilizing multi-whale optimization algorithms (WOA). This paper corrects errors in the equation of ohmic overpotential identified in previous HT-PEMFC literature and proposes two new correlations between parameters and operating temperature to achieve dynamic power output via WOAs. Real-time mission profile data, including the speed and altitude of a flight mission from YUL to YQL, are used to estimate power requirement profiles (max power: 3077 kW) and construct the extended cruise mission to reach the range with maximum payload. Furthermore, the study examines the design and configuration of liquid hydrogen cryogenic tanks, investigating their shape and displacement within the aircraft. It analyzes the conditions for minimum mass and volume of the entire system for payload, establishing a correlation between tank size and passenger capacity under different HT-PEMFC operating conditions. Additionally, various power split scenarios are simulated to estimate fuel consumption for the parallel hybrid electric system. Results indicate that HT-PEMFCs should avoid operating at high current density to maximize power output. Instead, operating at moderate current density can conserve fuel and optimize the correlation between payload and passenger capacity. This research provides a comprehensive analysis of performance enhancements from fuel systems, power systems, and power management strategies in new sustainable aircraft design.

I. Nomenclature

AFC	=	alkaline fuel cells
$ASME$	=	American Society of Mechanical Engineering
DL	=	Doping level of phosphoric acid
EM	=	electric motor
FC	=	fuel cell
HEP	=	hybrid-electric propulsion
$HT-PEMFC$	=	high temperature proton exchange membrane fuel cell
L/D	=	lift to drag
$Li-Ion$	=	Lithium Ion
PA	=	phosphoric acid (H_3PO_4)
PBI	=	polybenzimidazole
RH	=	relative humidity of an electrolyte
$SOFC$	=	solid oxide fuel cells
WOA	=	whale optimization algorithm
YQL	=	Lethbridge Airport, QC, Canada
YUL	=	Montréal-Pierre Elliott Trudeau International Airport, QC, Canada

*Graduate Student, Department of Aerospace Engineering, University of Michigan, Ann Arbor, Michigan 48109
†Assistant Professor, Department of Aerospace Engineering, University of Michigan, Ann Arbor, Michigan 48109, AIAA Senior Member.

II. Introduction

With increasing awareness of global warming and greenhouse gas emissions, the European Commission and Aerospace Industries Association have mandated that commercial aviation manufacturers achieve net-zero carbon emissions by 2050 [1]. Extensive research has been conducted on sustainable energy alternatives in aviation, such as lithium-ion (Li-Ion) batteries, hydrogen, and fuel cells to replace traditional jet fuel [2–8].

A. Previous Research and Challenges

Pastra et al. [2] examined the benefits of integrating polymer electrolyte membrane hydrogen fuel cells (PEMFC) and combinations of PEMFCs with Li-Ion batteries. Cinar et al. [9] investigated the design parameters of hybrid electric regional aircraft, demonstrating significant fuel savings with a parallel hybrid electric architecture compared to advanced conventional counterparts, when the energy and power management of the hybrid system was optimized during the aircraft sizing process. Troeltsch et al. [3] designed a long-range sustainable aircraft featuring liquid hydrogen (Hyliner 2.0), which, despite having a 9% higher energy consumption than conventional aircraft, only emits water, making it more environmentally friendly than burning kerosene.

However, several challenges remain. Clark et al. [4] found that the energy capacity of Li-Ion batteries in all-electric general aircraft could decay by up to 25% after one year of operation. Onorato et al.[8] highlighted that the substantial volume required for hydrogen fuel storage reduces the performance of hydrogen-powered aircraft, and discussed potential solutions for integrating hydrogen tanks in short-, medium-, and long-range aircraft. These studies underscore the potential of new sustainable aircraft designs, but also reveal significant challenges related to power source selection, fuel storage, and power management.

Sustainable energy sources, integral to new sustainable aircraft design, offer diverse properties with distinct advantages and disadvantages, as shown in Fig. 1. Li-Ion batteries are widely used due to their favorable gravimetric power density (specific power); however, their lower gravimetric energy density (specific energy) compared to fuel cells, as shown in Fig. 2 leads to significant increase in aircraft takeoff gross weight as well as empty weight. Additionally, the charging rate limitations of batteries can lead to longer than desired charging times at the gate [10]. Therefore, unless significant technological advancements occur rapidly, Li-Ion batteries may not be an appropriate candidate for the main power source of sustainable aircraft.

B. Focus of the Current Research

This research focuses on hydrogen and fuel cells as potential sustainable energy and power source options for aircraft. Hydrogen, as a fuel source, offers higher gravimetric energy density than both jet fuel and the state-of-the-art Li-Ion batteries (as shown in Fig. 2) and has a short refueling time (4 to 7 minutes [11]), similar to conventional vehicles. Fuel cells, as a power source, have better gravimetric energy density [12] and a longer lifetime than Li-Ion batteries [13]. For example, the U.S. Department of Energy predicts that the lifetime of fuel cell stacks in vehicles could reach 200,000 miles, whereas the lifetime of Li-Ion batteries in vehicles is mandated to be at least 100,000 miles. Additionally, the only emission from fuel cells is pure water [14]. Thus, this study investigates the implementation of hydrogen and fuel cells in new sustainable aircraft designs.

In real-world applications, ZeroAvia achieved a 10-minute mission of the first hydrogen-powered flight using the Dornier 228 in January 2023 [16]. They plan to deliver commercial flights with 9-19 seats by 2025 and regional aircraft like the Dash 8 series and ATR42/72 by 2027 [16]. Additionally, Universal Hydrogen flew the largest hydrogen fuel cell-powered airplane, a Dash 8 Q300 with 40 passenger seats, for 15 minutes in May 2023 [17]. Thus, fuel cells, particularly HT-PEMFCs, show great potential as the power source for future hydrogen-powered aircraft.

C. Comparison of Hydrogen Fuel Cells for Aviation Applications

There are multiple types of fuel cells, such as PEMFC, solid oxide fuel cells (SOFC), and alkaline fuel cells (AFC). PEMFC and SOFC are the most widely used globally due to their technological maturity [18]. SOFCs have good longevity and high efficiency, but their long start-up times and limited shutdown cycles [18, 19] make them more suitable for stationary power generation rather than aircraft. In contrast, PEMFCs are more appropriate for aircraft applications due to their quick start-up times, good dynamic behaviors, and high power density [18].

Within the PEMFC category, there are two types: low-temperature PEMFC (LT-PEMFC) and high-temperature PEMFC (HT-PEMFC). Despite both being PEMFCs, the differences between them are in operational conditions, properties, and structures [18]. LT-PEMFCs operate at temperatures between 60°C and 90°C, while HT-PEMFCs

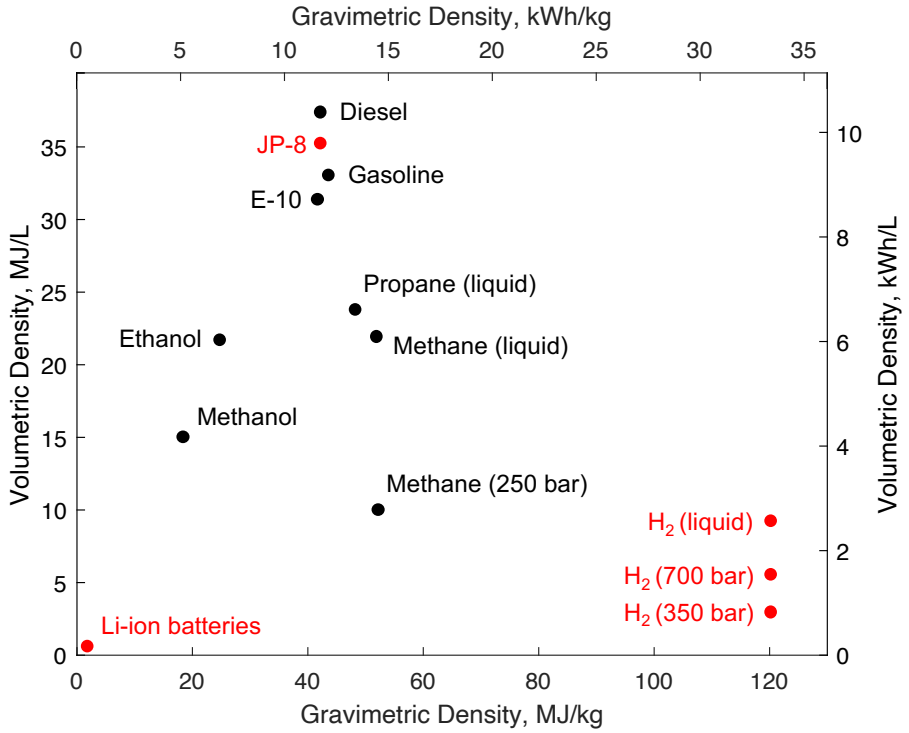

Fig. 1 Comparison of specific energy and energy density for several fuel types [15].

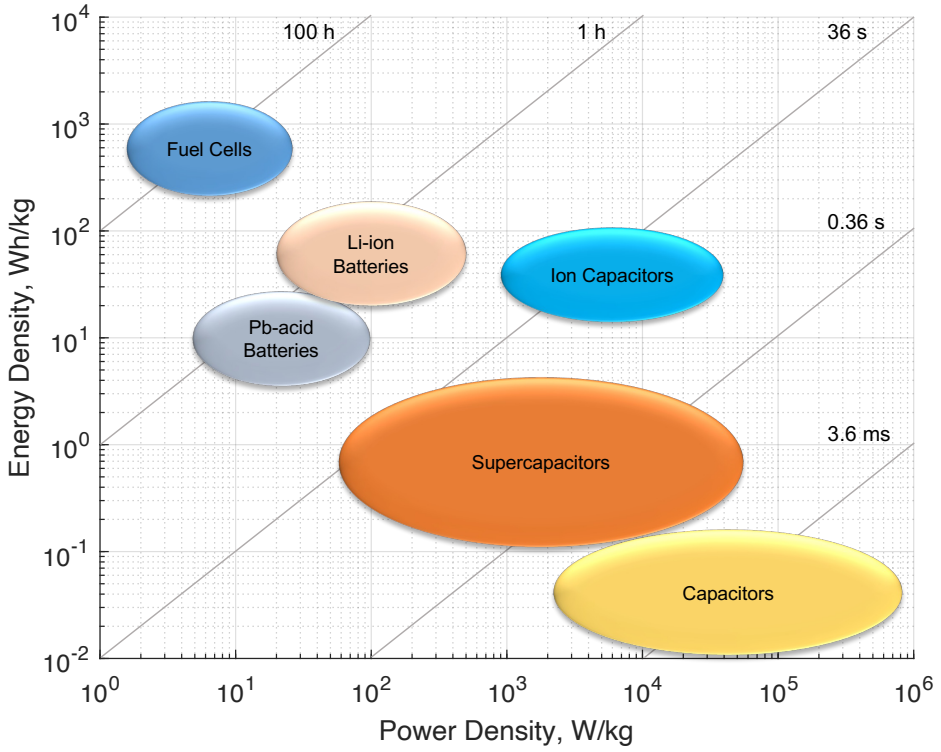

Fig. 2 Comparison of gravimetric energy and power density of various battery types and fuel cells [12].

operate between 130°C and 180°C. LT-PEMFCs use a Nafion membrane, whereas HT-PEMFCs utilize a phosphoric acid-doped polybenzimidazole (PA-PBI) membrane. Additionally, their configurations require different auxiliary devices, such as humidifiers and heat exchangers, to support performance.

There are three primary reasons for selecting HT-PEMFCs as the power source for this study instead of LT-PEMFCs. Kazula et al. [20] presented several benefits of HT-PEMFC application in commercial aviation. First, HT-PEMFCs have simpler water and heat management systems such as light compressors, no humidifiers and smaller radiators compared to LT-PEMFCs, which reduces the overall weight of the aircraft. Second, the alternative catalyst for HT-PEMFCs (Fe-based) is cheaper than that for LT-PEMFCs (Pt-based), reducing the cost of the power system. Third, HT-PEMFCs have a higher CO tolerance (30000 ppm) compared to LT-PEMFCs (30 ppm), allowing better adaptation to environmental changes. Moreover, a report from Hypoint indicated that the system specific power of HT-PEMFCs is up to 1.8 kW/kg, higher than the current state-of-the-art LT-PEMFCs at 0.75 kW/kg [21].

D. Hydrogen Storage Considerations

Fuel cells require hydrogen as fuel, making hydrogen storage crucial for sustainable aircraft design due to weight restrictions. Generally, hydrogen is stored physically in liquid (LH2) or compressed gaseous (CGH2) forms [22]. The volumetric energy density of liquid hydrogen (8.5 MJ/L) is higher than that of gaseous hydrogen (2.9 to 4.8 MJ/L) [5]. The mass fraction of LH2 (30 to 90%) is also higher than CGH2 (1 to 15%), meaning LH2 requires much less volume and weight to store energy than CGH2, demonstrating its greater potential as an aviation fuel. For the structure of LH2 storage tanks, Winnefeld et al. [23] pointed out that the optimal shape is cylindrical with hemispheric or elliptical domes at both ends, maximizing the mass fraction of hydrogen stored. Hence, this research selected liquid hydrogen stored in cryogenic tanks with a cylindrical shape as the fuel source.

E. Hybrid Electric Propulsion (HEP) System

Hybrid electric propulsion (HEP) is considered an effective candidate for short- or medium-range aircraft [24]. There are five categories of HEP: Series Hybrid, Parallel Hybrid, Series/Parallel Hybrid, All Electric, and Turbo-electric, each with properties suited to different applications, energy efficiencies, and technical challenges [6]. This paper focuses solely on the parallel hybrid architecture, as it allows propelling power to be provided by the engine, fuel cells, or both, covering three general propulsion systems. With 0% power split, the system operates as conventional propulsion, and with 100% power split, it operates as all-electric propulsion. Series and series/parallel hybrid architectures are not considered due to their added weight from electric generators and oversized motors, which reduces propulsive efficiency [7].

F. Objectives and Scope of the Paper

This paper aims to model HT-PEMFCs in a parallel hybrid electric turboprop aircraft using optimization algorithms to predict performance. The goal is to achieve minimum fuel consumption through optimized energy management strategies. Additionally, this paper conducts comprehensive system-level investigations, including the power output of fuel cells at different operating conditions, the design and displacement of hydrogen tanks, and the trade-off between tank volume and passenger capacity.

III. Technical Approach

In this paper, the aircraft, propulsion system, and flight mission analysis were modeled using Matlab/Simulink. The performance of HT-PEMFC was simulated through electrochemical reactions. Measuring unknown parameters such as the charge transfer coefficient and exchange current density directly from experiments is challenging. Therefore, multi-whale optimization algorithms [25, 26] were employed to determine these parameters, ensuring that the model aligns with experimental data and estimates the maximum power output under the operational constraints of HT-PEMFC.

Furthermore, the real-time power requirement profile of the Dash 8 Q300 was calculated based on the law of conservation of energy, flight speed, altitude, and lift-to-drag (L/D) ratio. Using this power requirement, the scale of the fuel cells was determined to design the hydrogen tank, utilizing the method of Barron [27] in accordance with the Boiler and Pressure Vessel Code of the American Society of Mechanical Engineers (ASME) [28].

The paper also analyzed fuel consumption and conducted trade-off studies involving payload reduction in the electric propulsion system and hydrogen tank for different power split ratios. The analysis process is illustrated in Fig. 3.

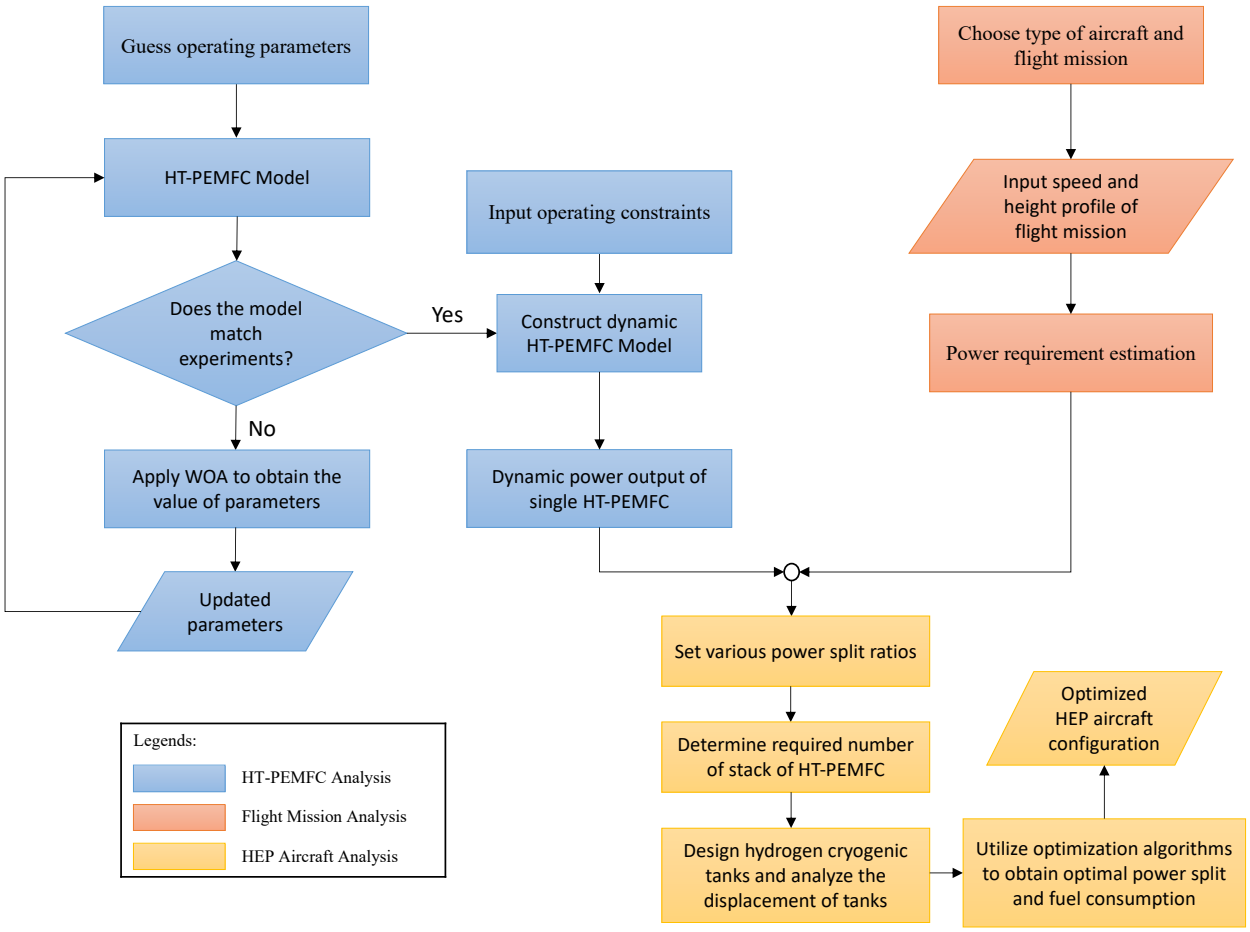

Fig. 3 Flowchart of technical approach for HEP aircraft design.

A. Electrochemical Modeling of HT-PEMFC

The main components of HT-PEMFC include an anode, a cathode and a PA-doped-PBI membrane, as shown in Fig. 4. The PA/PBI membrane provides efficient proton conductivity in the absence of moisture at temperatures above $100°C$. The electrochemcial reactions are given by the following Eq. (1) [14, 29]:

$$
\begin{aligned}
&\text{Anode (outside):} && \mathrm{H_{2(g)} \longrightarrow 2\,H^+ + 2\,e^-} \\
&\text{Anode (inside):} && \mathrm{H_2PO_4{}^- + H^+ \longrightarrow H_3PO_4} \\
&\text{Membrane:} && \mathrm{H_3PO_4 + PBI \longrightarrow H_2PO_4{}^- + PBI \cdot H^+} \\
&\text{Cathode (inside):} && \mathrm{H_2PO_4{}^- + PBI \cdot H^+ \longrightarrow PBI + H^+} \\
&\text{Cathode (outside):} && \mathrm{2\,H^+ + 0.5\,O_{2(g)} + 2\,e^- \longrightarrow H_2O_{(g)}} \\
&\text{Overall reactions:} && \mathrm{H_{2(g)} + 0.5\,O_{2(g)} \longrightarrow H_2O_{(g)} + electricity + heat}
\end{aligned}
\tag{1}
$$

The following assumptions are adopted in this model:

1. Steady state and isothermal condition: The temperature of fuel cells can be controlled by an electric heating device.
2. Ideal gas: The operation of HT-PEMFC is not at high pressure.
3. Single phase condition: The operation temperature of HT-PEMFC is above $100°C$; therefore, only vapor is present.
4. No contact resistances between components: In normal situations, there is no contact between components, so the contact resistances is negligible.
5. Membrane is impermeable to hydrogen and oxygen: If the membrane is permeable, the hydrogen and oxygen will

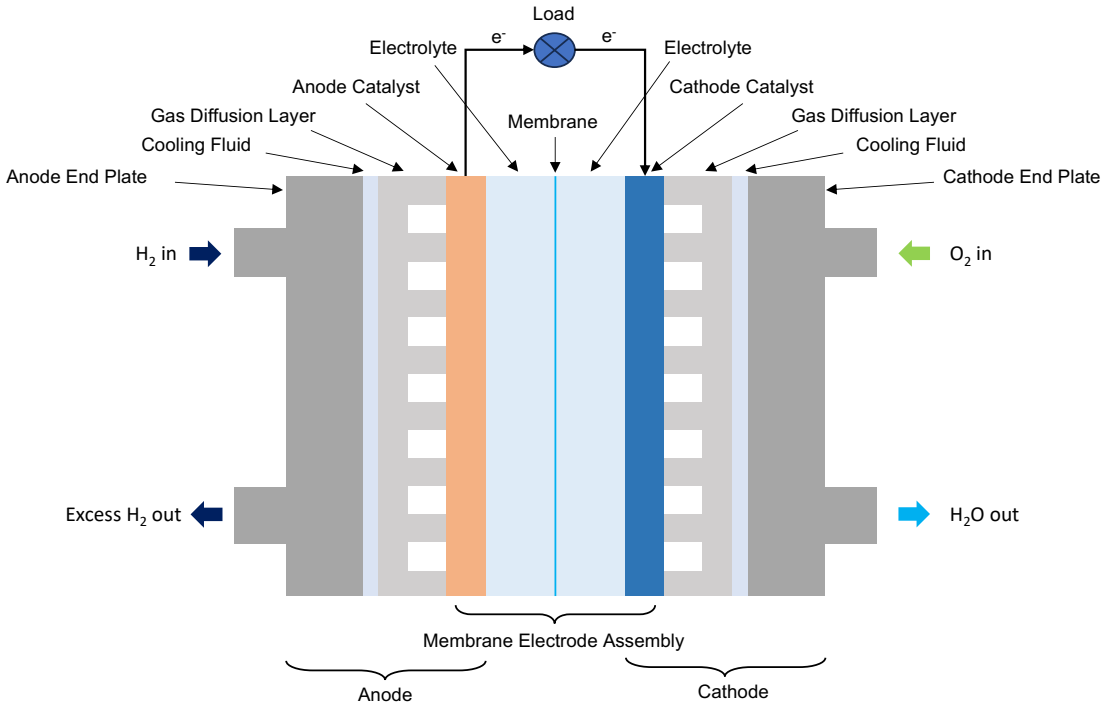

Fig. 4 General configuration of fuel cells.

diffuse to the other side, making the chemical reactions unpredictable.

As Eq. (1) shows, the chemical energies are transformed into electricity and exhaust heat. The generated electricity is transmitted to external electric loads via circuits, and the exhaust heat dissipates into the ambient environment. Based on electrochemistry and thermodynamics, if there are no external electric loads, the maximum reversible voltage of a single HT-PEMFC, E_{Nernst}, can be calculated using the Nernst equation [30] in Eq. (2).

$$E_{\text{Nernst}} = E^{\circ} + \frac{\Delta S}{n_e F}(T - T_0) + \frac{RT}{n_e F}\ln\left(\frac{p_{\text{H}_2} p_{\text{O}_2}^{0.5}}{p_{\text{H}_2\text{O}}}\right) \tag{2}$$

where E° is the ideal standard reference potential (298.15 K and 1 atm) which is 1.18 V for gaseous water [30]; ΔS is the molar change of the entropy of H_2O in 400 K < T < 500K (shown in Eq. (3) [31]); $n_e = 2$ is the number of electrons exchanged per hydrogen molecule; F is the Faraday's constant; T and T_0 are, respectively, the temperature of HT-PEMFC and the ambient; R is the ideal gas constant and p_{H_2}, p_{O_2} and $p_{\text{H}_2\text{O}}$ are the partial pressure of H_2, O_2, and H_2O (in atm), respectively.

$$\frac{\Delta S}{n_e} = f(T) = -18.449 - 0.01283\,T \quad J\,mol^{-1}\,K^{-1} \tag{3}$$

However, when an electric load is present, the actual output voltage of HT-PEMFC, U, is generally lower than the reversible potential due to three types of overpotential losses that affect the polarization curve: Activation Overpotential (E_{act}), Ohmic Overpotential (E_{ohm}), and Concentration Overpotential (E_{con}).

Activation Overpotential: The activation overpotential is the primary potential loss at low current density, resulting from overcoming the energy barrier of the slowest step of electrochemical reactions at the anode and cathode electrodes. It can be calculated using the Tafel equation [32].

$$E_{\text{act}} = \frac{RT}{\alpha n_e F}\ln\frac{j + j_{\text{leak}}}{j_0} \tag{4}$$

where the α is the charge transfer coefficient; j is the current density; j_{leak} is the leak current density due to internal current and reactant leaking and j_0 is the exchange current density, which can be represented by [33]:

$$j_0 = j_0^{H_3PO_4} - \exp\left(4.16(1 - \varepsilon_{PBI})\right) \tag{5}$$

$$\varepsilon_{PBI} = \left(\frac{4.81}{DL - 2} + 1\right)^{-1} \tag{6}$$

$$j_0^{H_3PO_4} = \exp\left(3.509 - 2139\, T^{-1}\right) \tag{7}$$

where $j_0^{H_3PO_4}$ is the exchange current density. Eq. (7) shows the value related to temperature in the case of 85 wt%H_3PO_4 [33]. ε_{PBI} is the volume fraction of amorphous phosphoric acid in the membrane. Because there are two bounding sites for PA in PBI membrane, the number of PA in the membrane should be subtracted by 2. DL is doping level, which is the number of phosphoric acid doping in every PBI unit.

Combining Equations (5) to (7), the exchange current density, j_0 can be rewritten as Eq. (8):

$$j_0 = \exp\left(3.509 - 2139\, T^{-1}\right) - \exp\left(4.16\left(1 - \left(\frac{4.81}{DL - 2} + 1\right)^{-1}\right)\right) \tag{8}$$

Ohmic Overpotential: Based on the transmission resistance of proton and electron through a membrane, the ohmic overpotential across a membrane can be derived as [34]:

$$E_{\text{ohm}} = j\,\frac{t_{\text{mem}}}{\sigma_{\text{mem}}} \tag{9}$$

here, t_{mem} represents the thickness of membrane and σ_{mem} represents the proton conductivity of membrane. σ_{mem} can be determined by an Arrhenius equation dependent on doping level of PA, relative humidity and operation temperature of HT-PEMFC[34, 35].

$$\sigma_{\text{mem}} = \frac{AB}{T}\exp\left(\frac{-E_{\text{a}}}{RT}\right) \tag{10}$$

where E_{a} represents the activation energy of a membrane ($J\ mol^{-1}$); A and B represent the pre-exponential factor for the doping level and humidity, respectively, which are fitted from experimental data[34, 36].

$$E_{\text{a}} = -619.6\ DL + 21750 \tag{11}$$

$$A = 168\ DL^3 - 6324\ DL^2 + 65750\ DL + 8460 \tag{12}$$

$$B = \begin{cases} 1 + (0.01704\,T - 4.767)\ RH, & 373.15K \le T \le 413.15K \\ 1 + (0.1432\,T - 56.89)\ RH, & 413.15K < T \le 453.15K \\ 1 + (0.7\,T - 309.2)\ RH, & 413.15K < T \le 473.15K \end{cases} \tag{13}$$

where DL denotes the doping level of PA; RH denotes the relative humidity of the electrolyte.

Concentration Overpotential: Concentration overpotential is caused by the slowness of mass transport and inadequate reactant supply during high current demand. It can be determined using the Butler-Volmer and Nernst equations [32, 37]:

$$E_{\text{con}} = \left(1 + \frac{1}{\alpha}\right)\frac{RT}{n_e F}\ln\frac{j_{\text{L}}}{j_{\text{L}} - j} \tag{14}$$

where j_{L} represents the limiting current density.

According to the above overpotentials, the actual voltage output of single HT-PEMFC, U, is given by Ref. [32]:

$$U = E_{\text{Nernst}} - E_{\text{act}} - E_{\text{ohm}} - E_{\text{con}} \tag{15}$$

Substituting Equations (4), (9) and (14) into Eq. (15, the U can be rewritten to be

$$U = E_{\text{Nernst}} - \left(\frac{RT}{\alpha n_e F} \ln \frac{j + j_{\text{leak}}}{j_0} + j \frac{t_{\text{mem}}}{\sigma_{\text{mem}}} + \left(1 + \frac{1}{\alpha}\right) \frac{RT}{n_e F} \ln \frac{j_{\text{L}}}{j_{\text{L}} - j} \right) \tag{16}$$

The power output and energy efficiency of the HT-PEMFC can be expressed by Ref. [32, 38]:

$$P_{\text{FC}} = V_{\text{FC}}\, I_{\text{FC}} = U j A_0 \tag{17}$$

$$\eta_{\text{FC}} = \frac{P_{\text{FC}}}{-\Delta \dot{H}} \tag{18}$$

where V_{FC} is the voltage output of fuel cells; I_{FC} is the current of fuel cells; A_0 is the effective area of the electrode; $-\Delta \dot{H}$ is the rate of overall generated energy of the electrochemical reaction, which can be determined by Ref.[32, 38]:

$$-\Delta \dot{H} = -\dot{q}_{\text{H}_2}\, \Delta H = -\frac{j A_0}{n_e F}\, \Delta H \tag{19}$$

where $\dot{q}_{\text{H}_2}$ is the hydrogen consumption rate, and ΔH is the total enthalpy variation for the hydrogen and oxygen reactions. The ΔH is equal to 285.83 kJ mol^{-1} for the exhaust water as liquid, and 241.82 kJ mol^{-1} as vapor.

Based on Equations (17) to (19), the theoretical hydrogen consumption rate (kg/s) and the energy efficiency of the HT-PEMFC can be rewritten to be:

$$\dot{q}_{\text{H}_2} = \frac{1}{n_e F}\, j A_0 = 1.05 \times 10^{-8} \times j A_0 \tag{20}$$

$$\eta_{\text{FC}} = \frac{U n_e F}{\Delta H} \tag{21}$$

B. Whale Optimization Algorithms

To explore the impact of parameters on the performance of parallel hybrid propulsion systems in aircraft, multi-whale optimization algorithms (WOA) [25, 26] were employed. WOA is a nature-inspired meta-heuristic optimization algorithm that mimics the hunting behaviors of humpback whales to locate optimal system parameters. This algorithm offers several advantages: it relies on simple concepts, avoids local optima, and operates without requiring gradient information. Fig. 5 illustrates the WOA procedure for achieving optimal results. The algorithm employs three methods to search for the best fitness of agents. Exploitation phase: (i) shrinking encircling mechanism and (ii) spiral updating position. Exploration phase: (iii) the search for prey. During the exploitation phase, equal probability is assumed for choosing between the shrinking encircling mechanism and spiral updating position.

For the shrinking encircling mechanism, the mathematical model can be presented by:

$$\vec{X}(t+1) = \vec{X}^*(t) - \vec{A} \cdot \vec{D} \text{ and } |\vec{A}| \leq 1 \tag{22}$$

$$\vec{A} = 2\vec{a} \cdot \vec{r} - \vec{a} \tag{23}$$

$$\vec{D} = |\vec{C}\vec{X}^*(t) - \vec{X}(t)| \tag{24}$$

$$\vec{C} = 2 \cdot \vec{r} \tag{25}$$

where the vector $\vec{X}$ is the position vector; $\vec{X}^*$ is the current best fitness of the search agent, which can be updated if a better solution is calculated in each iteration; $\vec{A}$ and $\vec{C}$ are the position vectors for the adjusted distance vector, $\vec{D}$; $\vec{a}$ is the factor vector linearly decreasing from 2 to 0 over a given number of iterations; and $\vec{r}$ is a random vector in the range of [0,1].

As $\vec{a}$ linearly decreases to 0 over the iterations, $\vec{A}$ will also reduce based on Eq. (23). When $|\vec{A}| \leq 1$, it ensures that the new position of a search agent will be located between the original position of the agent and the current best position of the search agent, thereby achieving the shrinking encircling mechanism.

For the spiral updating position, the mathematical model can be represented as:

$$\vec{X}(t+1) = \vec{D'} \cdot e^{bl} \cdot cos(2\pi l) + \vec{X^*}(t) \tag{26}$$

$$\vec{D'} = |\vec{X^*}(t) - \vec{X}(t)| \tag{27}$$

where $\vec{D'}$ is the distance between the search agent and the current best solution; b is the constant for shaping the logarithmic spiral; and l is a random number between -1 and 1, which constructs the spiral updating position.

In the exploitation phase, the mathematical model for the search for prey can be represented as:

$$\vec{D} = |\vec{C}\vec{X}_{rand}(t) - \vec{X}(t)| \tag{28}$$

$$\vec{X}(t+1) = \vec{X}_{rand}(t) - \vec{A} \cdot \vec{D} \text{ and } |\vec{A}| > 1 \tag{29}$$

where $\vec{X}_{rand}$ is a random position vector chosen from the current search agent position, and $|\vec{A}| \geq 1$ represents the exploration of search agents to do the global search, which is the mechanism of search for prey.

Combining the Equations (22), (26) and (29), the behavior mechanism of WOA can be demonstrated by:

$$\vec{X}(t+1) = \begin{cases} \vec{X^*}(t) - \vec{A} \cdot \vec{D} & if\ p < 0.5 \quad \text{and } |\vec{A}| \leq 1 \\ \vec{X}_{rand}(t) - \vec{A} \cdot \vec{D} & if\ p < 0.5 \quad \text{and } |\vec{A}| > 1 \\ \vec{D'} \cdot e^{bl} \cdot cos(2\pi l) + \vec{X^*}(t) & if\ p \geq 0.5 \end{cases} \tag{30}$$

where p is the random probability in [0,1] and the overall procedure of WOA is shown in Fig. 5

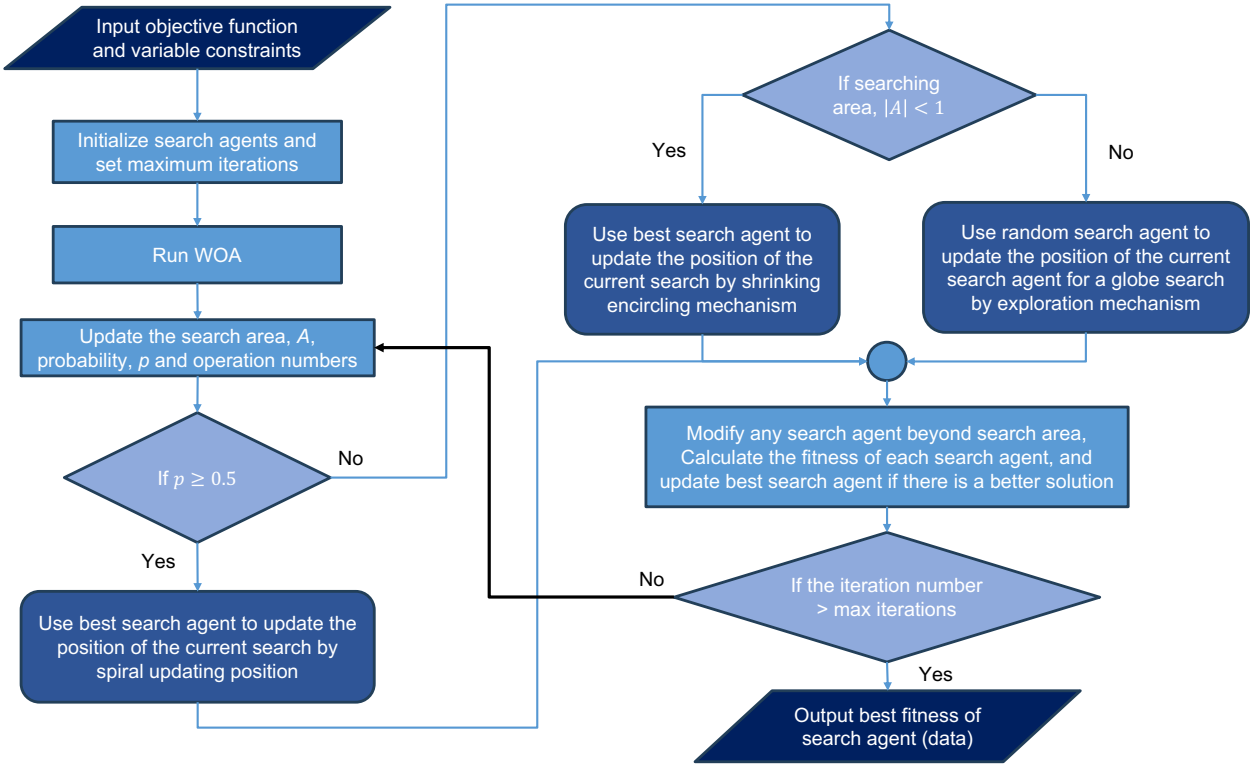

Fig. 5 The flow chart of the WOA algorithm.

C. Flight Mission Analysis

Hydrogen fuel cells are considered suitable for short and mid-range flight missions [24]. Recently, ZeroAvia and Universal Hydrogen have implemented fuel cells on regional turboprop aircraft, namely the Dornier 228 and Dash 8 Q300, respectively, for testing purposes. In this study, the flight mission selected for analysis is the Dash 8 Q300 route from YUL to YQL operated by Air Inuit, utilizing real-time speed and altitude data as references to estimate thrust and power requirements [39]. Following validation against existing literature and simulation results, the study extended cruise time at specific altitudes and speeds, iterating until the maximum payload range was achieved.

1. Dash 8 Q300 Specification

Table 1 outlines the specifications of the Dash 8 Q300 operated by Air Inuit and sourced from aviation databases [40–42]. The maximum takeoff weight (MTOW) is 19,000 kg, the operational empty weight (OEW) is 11,820 lbs, and the maximum payload capacity is 5,680 lbs. These data serve as a baseline for trade-off studies involving payload reduction strategies for integrating fuel cells, hydrogen tanks, and other subsystems.

Table 1 Specifications of de Havilland Dash 8 Q300

Specifications	Value	Unit
Engines	2	PW123
MTOW	19000	kg
MZFW	17500	kg
OEW	11820	kg
Maximum payload	5680	kg
Crews	2	people
Passenger Capacity	50	people
Aspect Ratio	13.36	–
Wing span	2.7	m
Cruise Speed	520	km/h
Range with max payload	1500	km

2. Lift-to-Drag Ratio Estimation

The Lift-to-Drag ratio (L/D) is essential for constructing the power requirement profile of an aircraft. However, publicly available data for every aircraft type is limited. To address this, Sforza [43] proposed a method to calculate the $(L/D)_{max}$ in subsonic cruise, requiring only the aspect ratio, flight Mach number, and mean aerodynamic chord (c_{mac}). It can be estimated by the following equation:

$$Re_{mac} \approx 7.093 \times 10^6 \, c_{mac} M [1 - 0.5(z/23500)^{0.7}] \tag{31}$$

$$(L/D)_{max} = 0.321 \left(AR^2 Re_{mac}\right)^{3/16} \left(1 + 3.6AR^{-9/4}\right)^{-1/2} \tag{32}$$

where c_{mac} is the mean aerodynamic chord of the wing, which can be estimated by the aircraft wetted area S_w and wing span b [43]; M Mach number; z is altitude in ft in the range [0, 50000] and AR is aspect ratio. The $(L/D)_{max}$ in subsonic cruise of Dash 8 Q300 can be calculated by the specifications in Table 1 and Equations (31) and (32).

3. Power Requirement Estimation

The power requirement analysis of an energy-based mission is based on the law of conservation of energy, shown in Equations (33) and (34) [44]. The power provided by engines is equal to the power requirement to overcome the drag and change the speed and altitude of flight.

$$TV = DV + \frac{d}{dt}(KE + PE) \tag{33}$$

$$TV = DV + \left(mg\frac{dh}{dt} + mV\frac{dV}{dt}\right) \tag{34}$$

where T represents the thrust of engine; V represents the speed of the flight; D represents the drag of the flight; KE represents the kinetic energy of the flight; PE represents the potential energy of the flight; m represents the mass of the flight; g represents the gravitational acceleration; h represents the altitude of the flight; dh/dt and dV/dt are the rate of climb and acceleration of the flight, respectively.

Therefore, given the lift-to-drag ratio, the altitude, and the speed of the flight for each point in the mission, the power requirement, P_{req}, can be calculated using Eq. (35):

$$P_{\text{req}} = TV = DV + \left(mg\frac{dh}{dt} + mV\frac{dV}{dt}\right) \tag{35}$$

With estimated power requirement at each point, the total energy requirement of the mission can be determined as:

$$E_{\text{req}} = \sum_{i=1}^{n-1} (P_{\text{req}})_i \, \Delta t_{i,i+1} \tag{36}$$

where n is the number of points in the mission profile, and $\Delta t_{i,i+1}$ is the time spent in between each consecutive point i and $i + 1$.

D. Parallel Hybrid Electric Turboprop Configuration

In hybrid-electric aircraft propulsion architectures, the parallel hybrid type offers distinct advantages over other hybrid configurations by eliminating the need for additional generators, which reduces overall system weight [6]. Moreover, the parallel HEP integrates electric motors and gas turbines individually connected to propellers, enabling independent control and power distribution. Therefore, this paper focuses on the parallel HEP configuration illustrated in Fig. 6 to analyze its impact on power distribution, overall propulsion system weight, and fuel consumption.

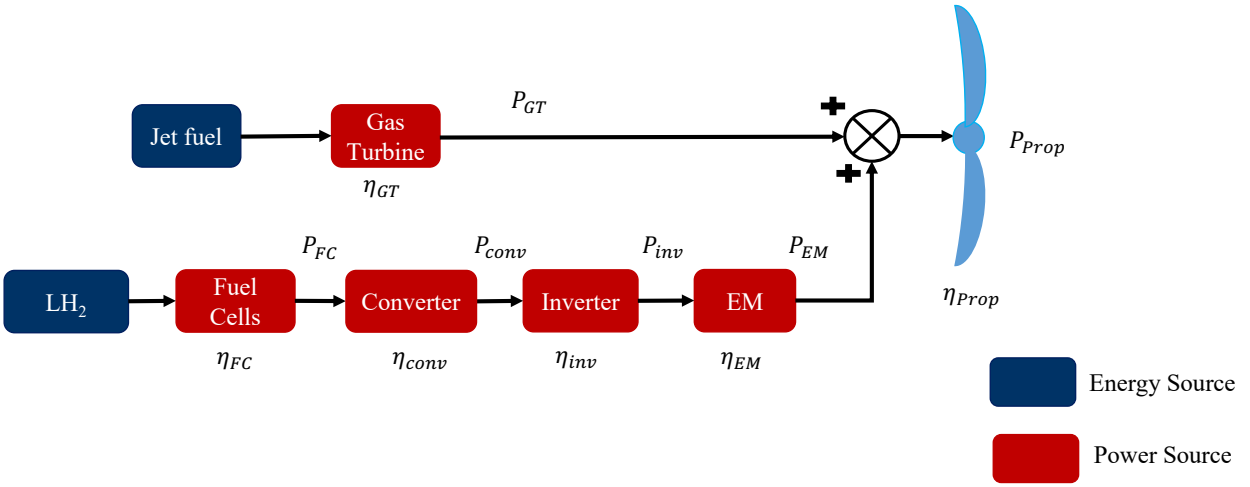

Fig. 6 The configuration of parallel hybrid electric turboprop.

To describe this architecture, we use the matrix-based framework first introduced by Cinar et. al. [45, 46] to describe various propulsion system architectures using "energy sources", "power sources", and "thrust sources", connected through "interdependency matrices." In this parallel HEP architecture, there are two energy sources: Jet fuel and Liquid hydrogen (LH_2), and five power sources: Gas turbines, Fuel cells, Converters, Inverters, and Electric motors (EM). The propeller is driven by both a gas turbine and an electric motor. The gas turbine is powered by jet fuel, while the fuel cells are powered by LH_2. The power output from the fuel cells goes through a converter and inverter to drive the

motor. The function of the converter is to stabilize the voltage output from the fuel cells and change the voltage level for different subsystems. Inverters are applied to convert the direct current (DC) generated by the fuel cells into alternating current (AC) to drive the electric motor, as most motors operate on AC [47]. To estimate the actual power generation of the fuel cells and subsystems, the power output of each component can be expressed as follows:

$$\begin{aligned} P_{EM} &= \lambda_H \times \frac{P_{prop}}{\eta_{prop}} \\ P_{inv} &= \frac{P_{EM}}{\eta_{EM}} &&= \lambda_H \times \frac{P_{prop}}{\eta_{prop}\,\eta_{EM}} \\ P_{conv} &= \frac{P_{inv}}{\eta_{inv}\,\eta_{subs}} &&= \lambda_H \times \frac{P_{prop}}{\eta_{prop}\,\eta_{EM}\,\eta_{inv}\,\eta_{subs}} \\ P_{FC} &= \frac{P_{conv}}{\eta_{conv}} &&= \lambda_H \times \frac{P_{prop}}{\eta_{prop}\,\eta_{EM}\,\eta_{inv}\,\eta_{subs}\,\eta_{conv}} \end{aligned} \tag{37}$$

where λ_H represents the power split ratio, defined as the ratio of electric power to the total thrust power requirement. The variables P_{prop}, P_{EM}, P_{inv}, P_{conv}, P_{FC}, η_{prop}, η_{EM}, η_{inv}, η_{conv}, and η_{FC} denote the power output and efficiency of propellers, electric motors, inverters, converters, and fuel cells, respectively. According to HyPoint's report [21], subsystems such as the compression and cooling system consume 9% of the power generated from fuel cells to support operations. Therefore, the efficiency of subsystems, η_{subs}, is defined as 0.91. Furthermore, Hall et al. demonstrated that the efficiency of DC-DC converters and DC-AC converters generally reaches around 98%. The efficiency of wiring is assumed to be 100%. Hence, based on Eq. (37), the actual power output requirement from fuel cells can be calculated.

To estimate the weight of subsystems, the specific power of each subsystem is applied. Spakovszky et al. [48] indicated that the specific power of state-of-the-art electric motors and converters/inverters is around 17 kW/kg and 20 kW/kg, respectively. In the HT-PEMFC system, it includes the compression, cooling, and control systems, which weigh 0.08, 0.07, and 0.01 kg/kW × gross power output from HT-PEMFC, respectively [21]. Therefore, by combining all the systems together, the weight configuration of the HEP aircraft can be shown as:

$$\begin{aligned} \text{MTOW} - \text{OEW} = W_{crews} + W_{payload} + W_{LH2,tank} + W_{LH2,fuel} + W_{jet,fuel} + W_{FC} \\ + W_{comp} + W_{cooling} + W_{control} + W_{conv} + W_{inv} + W_{EM} \end{aligned} \tag{38}$$

where MTOW is maximum take-off weight; OEW is operating empty weight; W_{crews}, $W_{payload}$, $W_{LH2,tank}$, $W_{LH2,fuel}$,$W_{jet,fuel}$, W_{FC}, W_{comp}, $W_{cooling}$, $W_{control}$, W_{conv}, W_{inv} and W_{EM} are the weight of the crews, payload, LH2 tank, LH2 fuel, jet fuel, HT-PEMFC, compression system for FC, cooling system for FC, control module for FC, converter, inverter and electric motor, respectively.

E. Liquid Hydrogen Cryogenic Tank Design

The foam-based insulation for the liquid hydrogen cryogenic tank, as described by Winnefeld et al. [23], was utilized in this study. This structure includes a tank liner, open-cell foam, multilayer aluminum, and mylar foil (MAAMF) vapor barrier and fairing. A tank liner is a specialized inner lining or barrier used to store and transport cryogenic liquids. Ahluwalia et al. [28] indicated three general materials used in cryogenic tank liners: Al 2219-T87, Al 5083-O, and SS 304/316. The thickness of the liner can be estimated by:

$$t_w = \frac{P_m R_i}{\eta_j \sigma_a - 0.6 P_m} \tag{39}$$

where t_w is the minimum required thickness of the liner, which includes an internal safety factor of 2 in Eq. 39; P_m is the maximum allowable internal design pressure of the liner material; R_i is the inner radius of the liner; η_j is the joint efficiency, generally equal to 0.9 for a fully single-welded butt joint; and σ_a is the maximum allowable stress of the liner material.

Open-cell foam is utilized to insulate against heat conductivity from the environment to maintain the temperature of LH2, which needs to be stored at 20 K. In this study, Rohacell foam is employed for its effective thermal insulation properties, featuring a thermal conductivity of approximately 5×10^{-3} W/m · K and a density of 35.24 kg/m^3 [23]. The study assumes a maximum boil-off rate of 0.2% per hour, with the external mean temperature around the tank at 300 K and the internal LH2 temperature at 20 K. The insulation thickness can be determined by [49]:

$$\dot{m}_{boil} = m_{\mathrm{H_2}} \times r_{boil} \tag{40}$$

$$\dot{Q}_{boil} = \dot{m}_{boil} \times (\Delta h_{\mathrm{H_2},evap} + \Delta h_{\mathrm{H_2},temp}) \tag{41}$$

$$\delta_{ins} = \frac{A_{ins}\,\kappa_{ins}}{\dot{Q}_{boil}} \times (T_{out} - T_{in}) \tag{42}$$

where the r_{boil} is the maximum boil-off rate; the m_{ceH2} is the mass of liquid hydrogen stored in the tank; $\dot{m}_{boil}$ is the mass flow of boil-off hydrogen per hour; $\Delta h_{\mathrm{H_2},evap}$ is the evaporation enthalpy change of liquid hydrogen at 1.5 bar, which is equal to 445.6 kJ/kg; $\Delta h_{\mathrm{H_2},temp}$ is the enthalpy change of temperature rising to boil off, which is equal to 490 kJ/kg; $\dot{Q}_{boil}$ is the rate of heat adsorption to boil off; T_{out} and T_{in} are the temperature outside and inside the tank, respectively; A_{ins} is the surface area of outer liner; κ_{ins} is the thermal conductivity of insulation material, and δ_{ins} is the insulation thickness.

The function of MAAMF in hydrogen tank is to provide effective barrier against gas hydrogen permeation and moisture ingress. MAAMF is consisted of layers of Mylar film sandwiched between layers of aluminum foil and additional layers such as dacron or glass net fabric to enhance mechanical stability or tear resistance. The surface density of MAAMF is 0.224 kg/m^2 [50] Additionally, the purpose of fairing outside the insulation is to protect it from the damage, which possesses the surface density of 1.304 kg/m^2 and the thickness of 1.57×10^{-2} m [23]. Based on the above information, the design of hydrogen cryogenic tank can be estimated like the weight and the volume.

IV. Results

In this research, our first objective is the development of a dynamic control model for High-Temperature Proton Exchange Membrane Fuel Cells (HT-PEMFC), aimed at predicting maximum power output based on dynamic variables such as hydrogen and oxygen supply rates and operating temperature with whale optimization algorithms. Our approach involves rectifying a previously wrong equation expression related to ohmic overpotential frequently reported in the literature. Additionally, we are establishing new correlations between the charge transfer coefficient and limiting current density relative to temperature variations, enhancing the model's accuracy in predicting the dynamic behaviors exhibited by HT-PEMFC systems. This model can simulate the performance of different HT-PEMFC designs, factoring in design variables including membrane thickness, doping levels, and effective reaction area.

Drawing from real-world flight requirements, specifically, the flight mission of Dash 8 Q300 from YUL to YQL, this paper intends to determine the optimal size of the HT-PEMFC stack and the volume of the hydrogen cryogenic tank for the aircraft. Our objective extends further to deriving an expression correlating passenger seating capacity with the volume of the hydrogen tank, based on the structural configuration of Dash 8 Q300. Furthermore, this study will analyze different power split scenarios, exploring varying power ratios between the PW123 engine and HT-PEMFC.

Ultimately, this study aims to deliver comprehensive insights into the integration of HT-PEMFC technology within the aviation field, offering potential design optimizations and operational strategies to achieve enhanced efficiency and sustainability in aircraft operations.

A. HT-PEMFC Model

1. Model Verification

Table 2 demonstrates the details of HT-PEMFC parameters to model the I-V curve. To validate the accuracy of the model, the modeling results are compared with three experimental data operating in different operating temperature: 413 K, 433 K, 453 K and 473K[51] as references. Through the WOA to estimate the value of required parameters, the results of polarization curves are obtained in Fig. 7, and power density and efficiency are shown in Fig. 8.

The model-predicted results shows great fitness with the experimental data with the statistic methods, R-squared (R^2) and adjusted R-squared (R^2) calculated in Table 3, to demonstrate that the model is highly reliable due to the values of regression analysis up to 99%.

According to Fig. 8, it is obvious that the power density and working efficiency increase as the rise of the operating temperature. The reason is that high temperature enhances the electrode kinetics for the oxygen and hydrogen reactions, increases the mass transfer of the reactants, and improves the membrane proton conductivity to reduce the ohmic

Table 2 Operating and design parameters in the HT-PEMFC modeling.

Parameters	Description	Value	Unit
F	Faraday constant	96485	$C\ mol^{-1}$
R	Universal gas constant	8.314	$J\ mol^{-1}\ K^{-1}$
n_e	Number of electron	2	–
T_0	Ambient temperature	298.15	K
T	Operating temperature	413, 433, 453, 473	K
E_0	Ideal standard potential	1.18	V
p_{H_2}	Partial pressure of hydrogen in anode	1	atm
p_{O_2}	Partial pressure of oxygen in cathode	0.21	atm
j_{leak}	Leak current density	0.0005	$A\ cm^{-2}$
α	Charge transfer coefficient	0.361, 0.383, 0.414, 0.445	–
DL	Doping level	11	–
RH	Relative humidity	0.38	%
j_L	Limiting current density	1.74, 1.88, 2.03, 2.13	$A\ cm^{-2}$
t_m	Thickness of membrane	0.005	cm

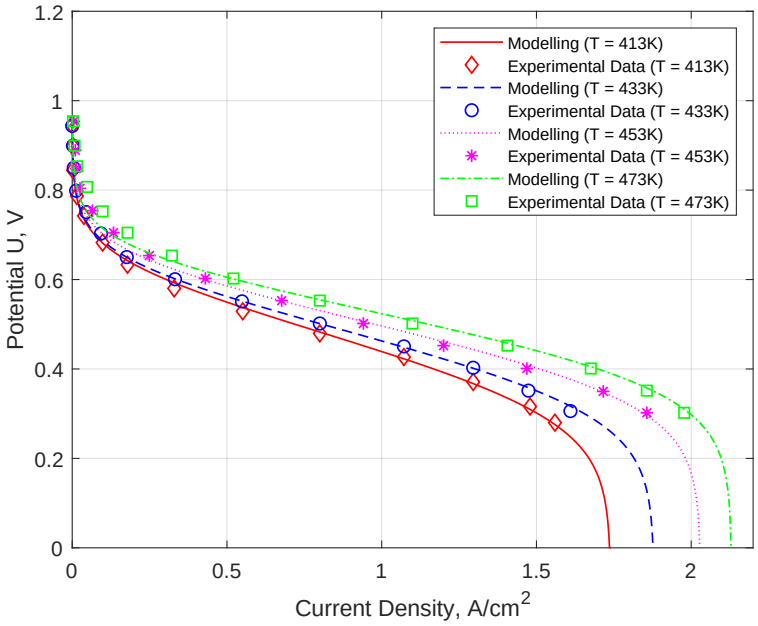

Fig. 7 Comparison between model predictions and experimental data[51, 52] at various operating temperature (operating anode/cathode pressure of 1 atm, 0.38% relative humidity of electrolyte and 11 doping level).

overpotential. Furthermore, the limiting current density(j_L) and charge transfer coefficient(α) rise with the increasing operating temperature, shown in Fig. 9. The enhancement of electrochemical reactions and mass transfer led HT-PEMFC to generate more electrons and obtain a higher charge transfer coefficient, which matches our modeling. Based on the results, this paper proposes two equations to express the correlation between limiting current density/charge transfer coefficient and operating temperature for dynamic controls in this case, respectively:

$$j_L = -2.5 \times 10^{-5}\ T^2 + 0.02875\ T - 5.873 \tag{43}$$

$$\alpha = 5.6 \times 10^{-6}\ T^2 - 0.003569\ T + 0.875 \tag{44}$$

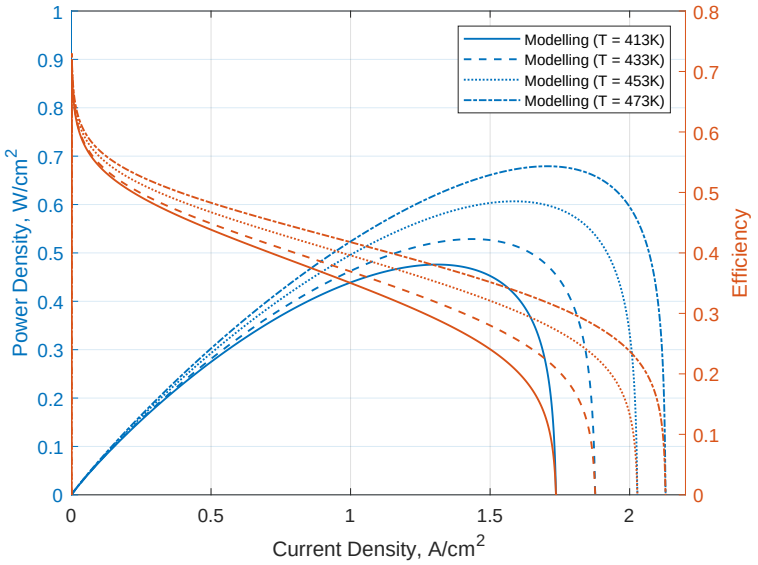

Fig. 8 The power density and efficiency of HT-PEMFC modeling at various operating temperature.

Table 3 Regression Analysis for different operating temperature of HT-PEMFC.

Model	R^2	*Adjusted* R^2
T = 413 K	99.6%	99.6%
T = 433 K	99.7%	99.7%
T = 453 K	99.0%	98.9%
T = 473 K	99.7%	99.6%

2. Operating and Design Variable Analysis

There are four operating variables (T, p_{H_2}, p_{O_2} and RH) and two design variables (t_m and DL) that influence the performance of HT-PEMFC. To investigate the sensitivity of each variable at different operating temperatures on HT-PEMFC performance, a fraction factorial design was employed to analyze their effects on power density output. The operating temperature is constrained within [413, 473] K, as typical operating temperatures range from approximately 413 to 453 K [20]. The inlet pressure of fuel is limited to [0.1, 5] atm, reflecting optimal operating pressures typically between 3 and 4 atm [53]. The constraint on the relative humidity of the electrolyte is [0.001, 0.05] due to the requirement for extremely low or even close to 0% humidity [54]. The thickness of the membrane is constrained to [2, 12]$\times 10^{-3}$ cm aligning with typical designs of PA-PBI membranes [55]. Lastly, the doping level is maintained around [1, 15]. While a higher doping level enhances PBI conductivity, excessively high levels can compromise membrane mechanical strength [29].

Fig. 10 illustrates the impact of various operating temperatures and design/operating variables on power density. At the specified operating temperatures from Table. 2, the power density output increases by 55% (0.478 to 0.741W/cm^2) as the temperature rises from 413 K to 473 K. This enhancement is attributed to the higher operating temperature, which improves theoretical open circuit voltage and electrochemical efficiency through increased ion conductivity and faster reaction kinetics.

In Fig. 8, it is observed that temperature significantly affects power density output. Based on Fig. 10a and Fig. 10b, increasing the inlet pressure of hydrogen and oxygen enhances power density, with hydrogen showing greater sensitivity compared to oxygen. For example, at a fixed operating temperature of 450 K, power density increases by 21% (0.558 to 0.677W/cm^2) as hydrogen pressure increases from 0.1 to 5 atm, whereas oxygen shows a 9% increase (0.616 to 0.676W/cm^2) under similar pressure changes. Thus, controlling hydrogen pressure is more critical for optimizing power output than controlling oxygen.

Fig. 10c shows that at an operating temperature of 450 K, varying the relative humidity of the electrolyte from 0.001

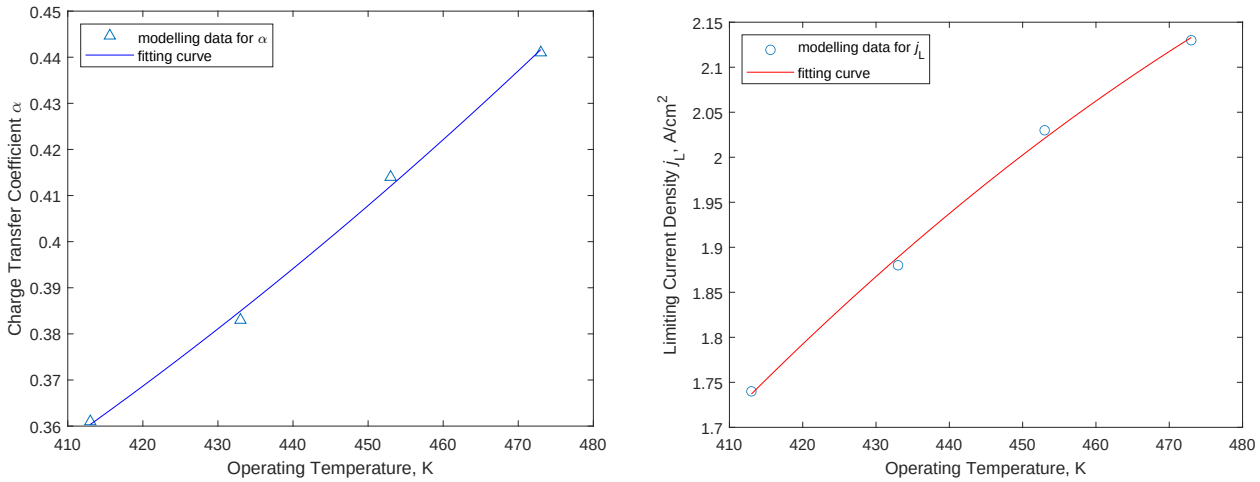

(a) The change of charge transfer coefficient, α. **(b) The change of limiting current density, j_L.**

Fig. 9 The fitting curve of the change of charge transfer coefficient and limiting current density at different operating temperatures.

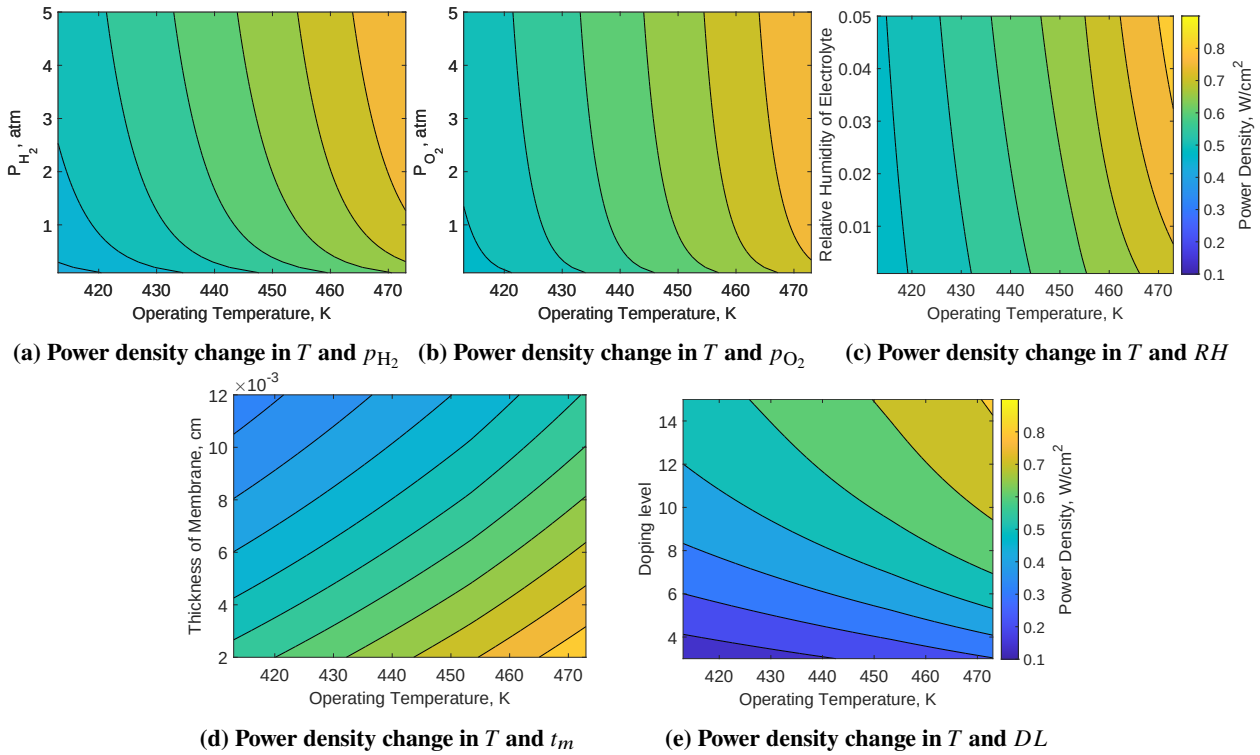

(a) Power density change in T and p_{H_2} **(b) Power density change in T and p_{O_2}** **(c) Power density change in T and RH**

(d) Power density change in T and t_m **(e) Power density change in T and DL**

Fig. 10 The change of power density with different values of temperature and operating/design variables.

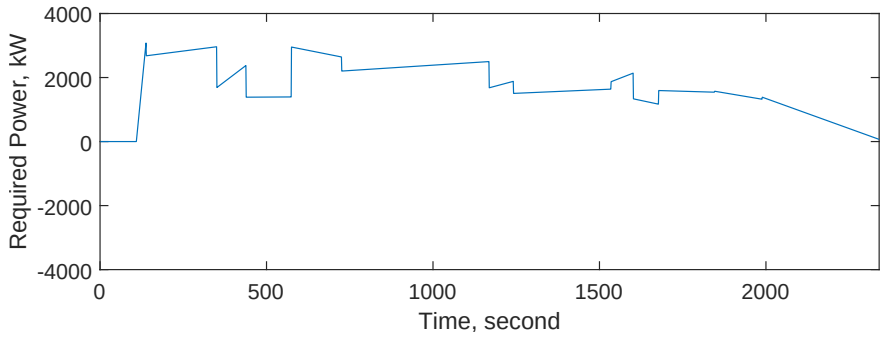

(a) The estimated power requirement profile of the mission.

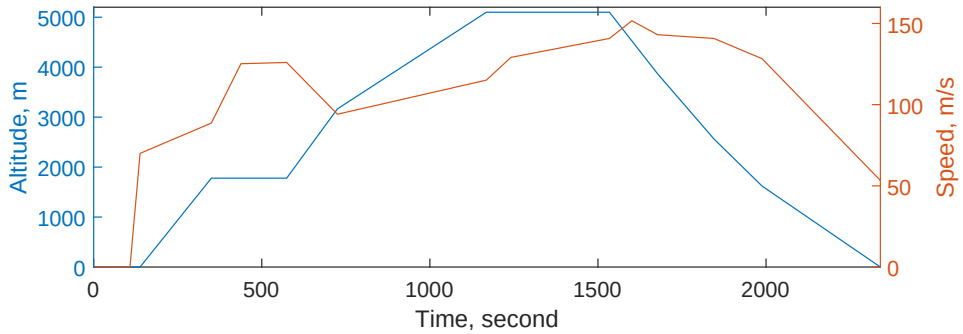

(b) The real-time speed and altitude profile of the mission.

Fig. 11 The power requirement profile of Dash 8 Q300 from YUL to YQL, based on the real-time speed and altitude data.

to 0.05 results in a modest 7% increase in power density output (0.624 to 0.668 W/cm^2). This minimal effect is due to the generally low relative humidity of the electrolyte, which limits its impact on fuel cell performance. Fig. 10d demonstrates that membrane thickness significantly influences power output. At an operating temperature of 450 K, increasing the membrane thickness from 2×10^{-3} to 12×10^{-3} cm decreases power density by 38% of power output (0.727 to 0.448 W/cm^2). This decrease occurs because thicker membranes increase ion resistance, leading to higher ohmic losses.

Lastly, Fig. 10e indicates that power density output is influenced most by doping level compared to other operating and design variables. At an operating temperature of 450 K, increasing the doping level from 3 to 15 results in a substantial 221% (0.218 to 0.700 W/cm^2)increase in power density his increase is attributed to enhanced proton conductivity in higher doping level membranes, effectively reducing ohmic losses. Based on the sensitivity analysis above, improving the performance of HT-PEMFC involves designing membranes with higher doping levels and thinner membranes, and operating at high temperatures and inlet pressures. Among them, doping level is the most critical factor affecting the performance of HT-PEMFC.

B. Power Requirement Profile in the Mission

Based on real-time speed and altitude data collected from a Dash 8 Q300 flight from YUL to YQL, the power requirement profile was determined using the principle of energy conservation, shown in Fig. 11. The peak power demand during this mission reached approximately 3077 kW, with an estimated energy consumption of around 862 kWh. Each of the Dash 8 Q300's two PW123 turboprop engines can produce a maximum power output of 1775 kW, totaling 3550 kW for both engines. Our estimation aligns with the PW123 specifications, demonstrating a reasonable margin and confirming the validity of our approach.

Due to the unavailability of publicly accessible fuel consumption data for validation over this short mission, this study extended the cruise duration to achieve the maximum payload range, detailed in Table. 1. An extended cruise mission profile was developed to estimate power requirements and fuel consumption, illustrated in Fig. 12. Calculations

based on maximum takeoff weight (MTOW) and maximum zero fuel weight (MZFW) yielded an estimated fuel mass of approximately 1500 kg with maximum payload. Our model predicted a fuel consumption of 1284 kg to cover a distance of 1500 km, corresponding to an energy consumption of 54930 MJ during the extended mission. The estimated fuel consumption aligns well with safety regulations, which typically saves 10% fuel for a reserve mission. Thus, only 1350 kg of the 1500 kg fuel was utilized for the 1500 km flight. The difference in fuel consumption between literature values and our model was 4.8%, indicating successful validation of our approach.

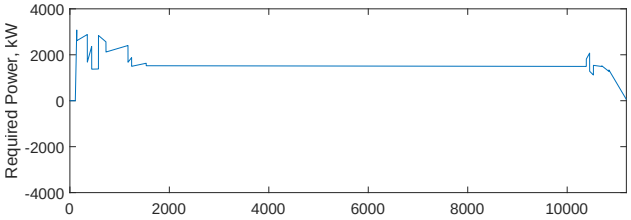

(a) The estimated power profile of the extended cruise mission.

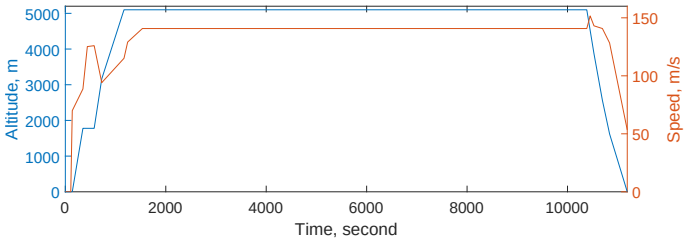

(b) The altitude and speed profile of the extended cruise mission.

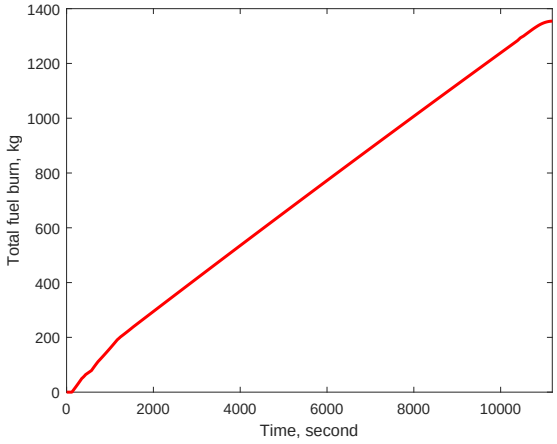

(c) Total fuel consumption along the time in extended cruise mission.

Fig. 12 The altitude/speed,estimated power and total fuel burn profile in the extended cruise mission modified from original YUL to YQL mission profile.

C. The weight and volume trade-off studies among hydrogen tanks, fuel cell systems and subsystems at 100% power split and full tank in the parallel hybrid system

In Fig. 8, it is observed that at a fixed temperature, increasing current density to maximize power output results in a corresponding decrease in efficiency. This trade-off impacts the weight balance between fuel cells and hydrogen tanks. For instance, operating fuel cells at maximum power output with fixed current density and voltage will reduce the efficiency. Although this approach requires fewer fuel cell stacks to meet power demands, it requires a larger hydrogen tank due to a higher fuel consumption rate and poor efficiency. On the contrary, operating at a lower current density to achieve lower power output improves efficiency. This strategy increases the number of fuel cell stacks needed to meet power requirements but allows for a smaller hydrogen tank for fuel storage. Therefore, this study investigates the weight trade-off between fuel cells and hydrogen tanks, crucial considerations in aircraft design where weight is a primary concern.

Initially, this paper integrates the operating conditions from HyPoint [21] into our model and its specifications to estimate the weight per cell. to assess HT-PEMFC performance and estimate cell weights. In a 20 kW module, 160 cells operate in series at 453 K and 250 kPa inlet pressure, resulting in a stack weight of 6.6 kg and an output voltage of 110 V. Based on these specifications, each cell is estimated to generate 125 W with a voltage of 0.7 V, a current density of 0.5 A/cm^2, a reaction area of 357 cm^2 and a weight of 41.25 g. The performance of HT-PEMFC using HyPoint's specifications is demonstrated in Fig. 13.

In addressing the structure and materials for the hydrogen tank, this study applied the total energy consumption estimated during the extended cruise mission, along with references to three commercial materials [28] and the structure of tank [23] to analyze the shape and material for the hydrogen tank. In this case, The chosen tank design incorporates foam insulation to maintain a boil-off rate of 0.2% per hour without requiring external power for hydrogen temperature control. Table. 4 shows that the empty tank weight using Al 5803-O or SS304/316 is 60.3% and 103% heavier than Al 2219-T87, respectively, with minimal volume differences (< 2%) among these materials. Therefore, this paper selected the Al 2219-T87 as the preferred material for the hydrogen tank.

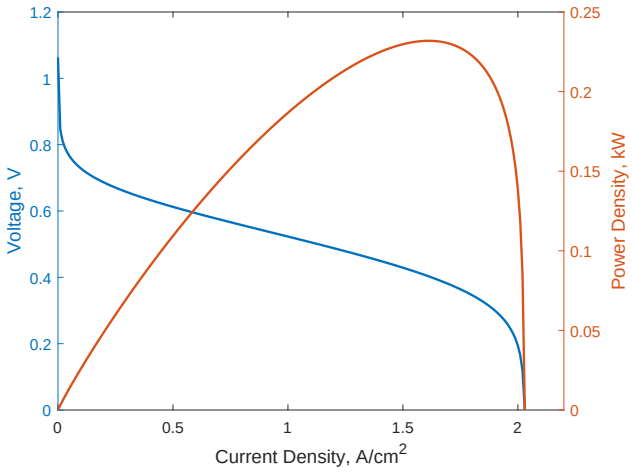

Fig. 13 The polarization curve and power output of HT-PEMFC modeling with HyPoint's specifications.

Table 4 The comparison of different material selections for a liquid hydrogen tank design with 6.5 m of tank length and carrying 495 kg of liquid hydrogen for extended cruise mission.

Materials	Al 2219-T87	Al 5803-O	SS304/316
Max allowable stress at 80 K, MPa	196.9	107	243
Density, kg/m^3	2.84×10^3	2.66×10^3	8×10^3
Thickness of liner, m	0.00341	0.00629	0.00276
Thickness of insulation, m	0.1325	0.1332	0.1323
Weight of tank, kg	325.8	522.4 (+60.3%)	662.3 (+103%)
Weight of full tank, kg	821.0	1017.6 (+23.9%)	1157.5 (+40%)
Volume of tank, L	12622	12854 (+1.8%)	12570 (-0.4%)
Diameter of tank, m	0.757	0.764	0.756

Next, the impact of hydrogen tank shape on weight and volume is analyzed by varying the cylinder length, illustrated in Fig. 14. The mass of the tank decreases as the length of the cylinder tank increases. However, it has marginal benefits once the length of the tank is around 4 meters, shown in Fig. 14a. This phenomenon arises because the liner's capacity remains fixed to store the same fuel volume, and the liner's thickness is primarily affected by its radius. Beyond a certain length, increasing the cylinder length only slightly affects the liner's radius, resulting in a slower decrease in liner weight. Moreover, Fig. 14b shows that a longer and thinner tank features a smaller radius but a larger volume.

Finally, this paper integrates the HT-PEMFC propulsion system with all subsystems, tanks, and fuel to conduct trade-off analyses of weight and volume among these components, shown in Fig. 15. Here, the power split is set at 100%, indicating that all power is supplied by fuel cells. In Fig. 15a, the result indicates that the minimum weight of the whole system with full tank occurs at the current density around 1.3 A/cm^2. This is attributed to the operational characteristics shown in Fig. 13, where lower current densities require a larger number of fuel cell stacks to meet power requirements, dominating system weight. And the fuel cell is operating at optimal efficiency, which can limit fuel demand, shown in Fig. 15f. Increasing current density reduces the number of required fuel cells to achieve power output, decreasing stack weight at the same time. However, this increase in current density also requires a larger tank and higher hydrogen consumption, leading to increased tank weight. Therefore, a trade-off exists between stack number and tank weight.

Then, around the condition of maximum current density, fuel cells experience concentration losses, which reduce power output and efficiency. Consequently, the increased demand for more fuel cell stacks and hydrogen results in a higher total system weight. This correlation between the weights of fuel cell stacks, tank, and fuel under varying operating conditions is explained in Fig. 15f. The total volume of the tank and fuel cells exhibits different behaviors compared to the overall system weight, illustrated in Fig. 15b. Moreover, Fig. 15c indicates that tank volume increases with higher current density or with a longer and thinner tank shape. At lower current densities (< 0.8 A/cm^2), the

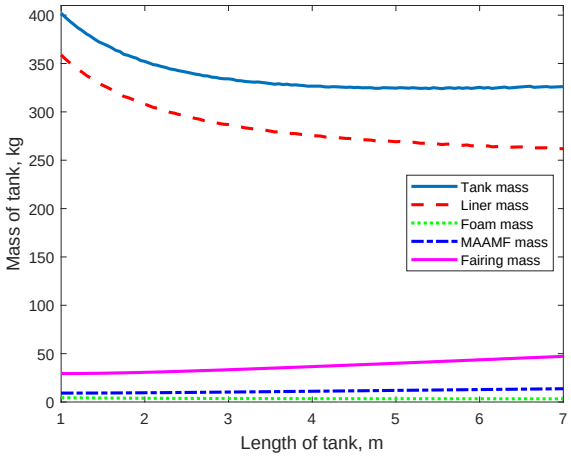

(a) The weight composition of the tank design with respect to different radii and lengths of the tank.

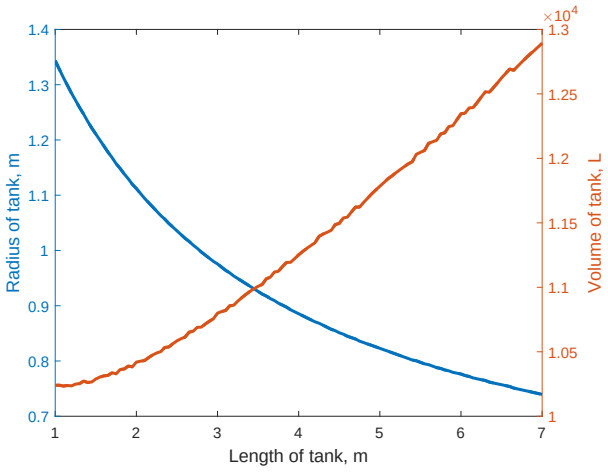

(b) The volume of the tank design with respect to different radii and lengths of the tank.

Fig. 14 The weight, volume, and shape analysis of the tank design with a full tank to complete the extended cruise mission.

Table 5 The weight, volume and remaining max payload estimation of the whole propulsion system at different operating conditions and with tank radius of 1.86 m.

Item	Case 1	Case 2	Case3	Case 4	Case 5
Current density, A/cm^2	0.6	0.9	1.1	1.3	1.6
Voltage, V	0.593	0.540	0.505	0.469	0.406
Power per cell, kW	0.127	0.174	0.199	0.218	0.232
Number of cells, unit	34641	25365	22175	20211	18985
Efficiency	0.473	0.431	0.403	0.374	0.324
Cylinder length, m	3	3.3	3.5	3.8	4.5
Total volume, L	14169	13815 (-2.5%)	14040 (-0.9%)	14579 (+2.9%)	16162 (+14%)
Total mass, kg	3513	3203 (-8.8%)	3127 (-10.9%)	3113 (-11.3%)	3208 (-8.6%)
Remaining max payload, kg	2168	2477 (+14.2%)	2553 (+17.7%)	2567 (+18.4%)	2472 (+14.0%)

system's high efficiency minimizes the need for a larger tank to store hydrogen. However, the additional fuel cell stacks increase system volume. The minimum volume occurs around a current density of 0.9 A/cm^{2}where fewer fuel cell stacks significantly reduce the volume occupied by them while maintaining good operational efficiency prevents rapid increases in tank volume. As current density increases, diminishing operational efficiency requires a larger tank volume for fuel storage, contributing to overall system volume growth. Hence, operating efficiency is crucial in determining tank volume requirements and overall system volume at higher current densities. Additionally, Fig. 15d shows the tank shape at different operating conditions.

Fig. 15e illustrates that the points of minimum system weight and minimum system volume do not coincide at the same operating conditions (1.3 A/cm^2 vs 0.9 A/cm^2). To visualize changes in weight and volume under different operating conditions, five points of current density ranging from 0.6 to 1.6 A/cm^2 were selected. These points are detailed in Table. 5 to demonstrate variations in weight and volume of the entire system.

The analysis shows that at the point of minimum weight (case 4), the payload capacity can be increased by an additional 18% weight (around 200 kg) compared to the case 1 condition. However, the system volume experiences a slight increase of 2.9%. Conversely, aiming for minimum volume (case 2) requires sacrificing some payload to accommodate more fuel cell stacks. In case 5, while the payload shows an improvement (+14%) compared to case 1, the system volume increases significantly (+14%), potentially impacting cabin capacity. Therefore, to balance weight and volume considerations, it is advisable to operate the fuel cell within an appropriate current density range, avoiding

extremes of low or high current density extraction. Additionally, the cylinder tank diameter is constrained to 1.86 m due to the dimensions of the Dash 8 Q300 cabin (1.95 m height and 2.51 m width), with an additional 0.1 m space allowance. Thus, the tank size is determined based on the radius and length of the cylinder tank.

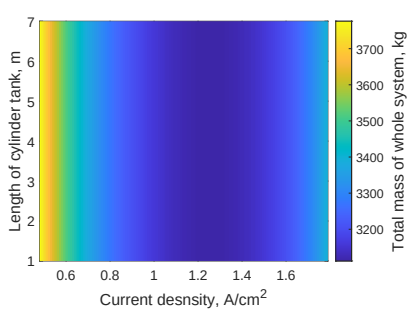

(a) The change of the total mass of the whole system.

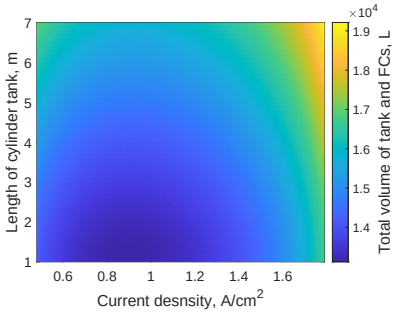

(b) The change of the total volume of tank and FCs.

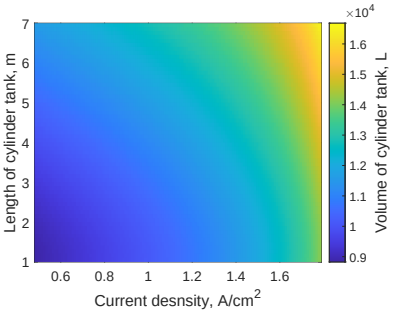

(c) The change of the volume of hydrogen tank.

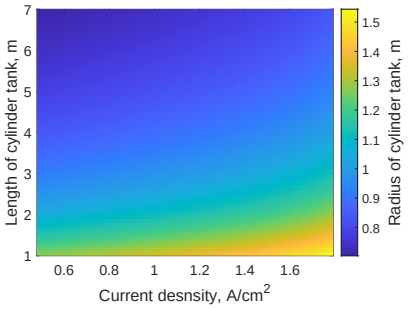

(d) The change of the shape of hydrogen tank.

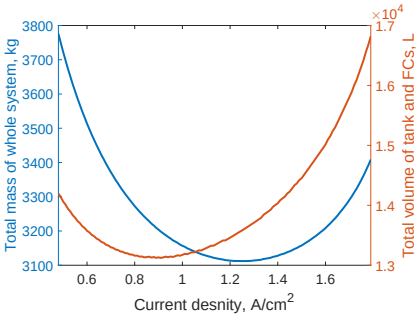

(e) The comparison of total mass volume of the system.

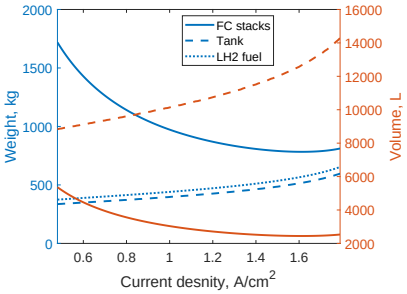

(f) The change of the weight of FCs, tank and LH2 fuel.

Fig. 15 The weight and volume analyses of the whole system at different operating conditions and 100% power split condition.

D. Fuel and Hydrogen Consumption and Fuel Cell Performance Under Various Power Split and Operating Conditions

Fig. 16 demonstrates the energy consumption rate across different operating current densities and power splits. In Fig. 16a, it is evident that at a 100% power split, operating at lower current densities such as 0.6 or 0.9 A/cm^2 results in significant energy savings compared to using jet fuel, attributed to the higher efficiency at lower current density conditions. However, this efficiency gain comes at the cost of increased system weight penalties. Conversely, higher current densities result in higher energy consumption due to lower efficiency, while with a slight reduction in system weight, given in Table. 5. Fig. 16b, Fig. 16c, and Fig. 16d similarly demonstrate that using jet fuel does not yield energy savings at lower current density conditions but does so at higher current densities. In hybrid conditions, as the power split decreases, the energy consumption rate increases for lower current densities, while higher current densities exhibit the opposite trend. At zero power split, indicating exclusive use of jet fuel, all lines align with jet fuel energy consumption rates.

Fig. 17 presents total energy consumption and fuel mass requirements across different power splits and current densities. At a 100% power split, the required fuel mass is minimized because of higher energy density of hydrogen compared to jet fuel (120 vs 42 MJ/kg). The result shows that the aircraft operating at 0.6 A/cm^2 current density condition can save around 1 to 5% energy concerning different power ratios. However, if it operates at a high current density like 1.6 A/cm^2 current density, its energy consumption can be up to 30% more than burning conventional jet fuel. Therefore, to optimize energy savings during missions, the system should be operated at lower current density conditions.

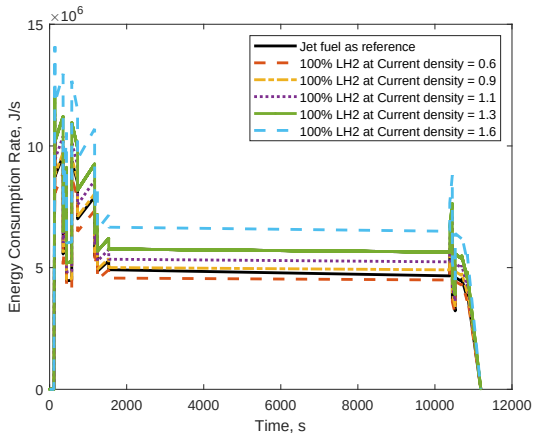

(a) At 100% power split, the energy consumption rate at different operating conditions.

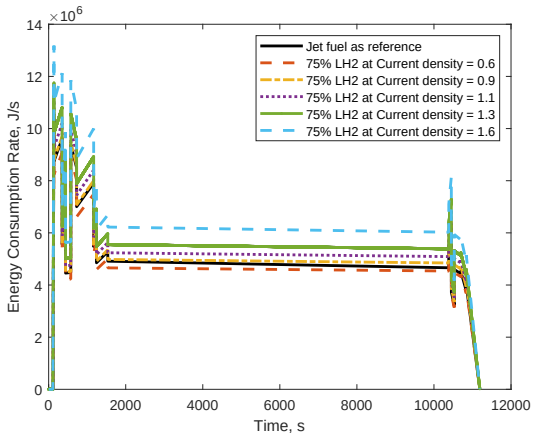

(b) At 75% power split, the energy consumption rate at different operating conditions.

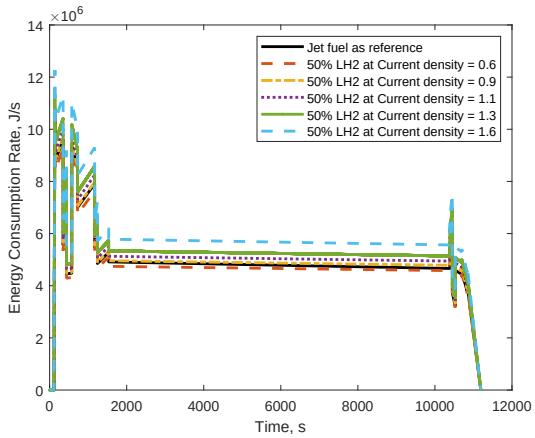

(c) At 50% power split, the energy consumption rate at different operating conditions.

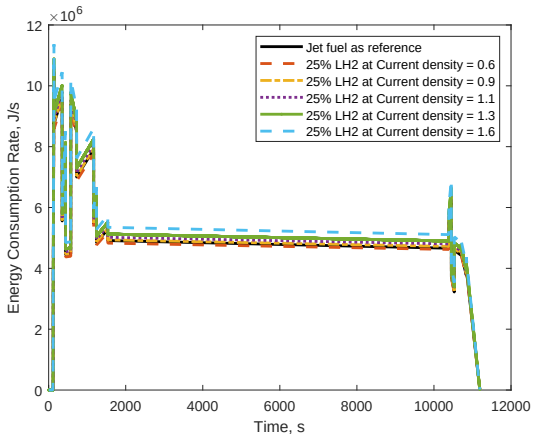

(d) At 25% power split, the energy consumption rate at different operating conditions.

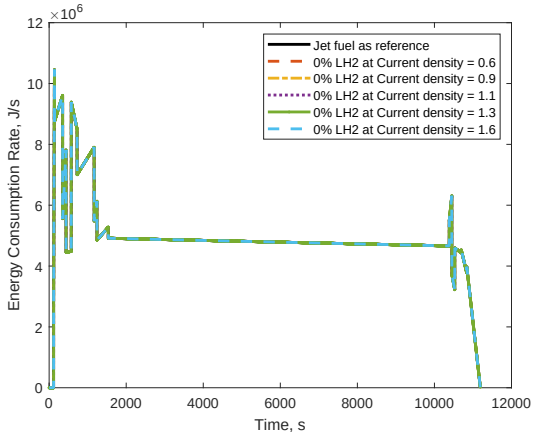

(e) At 0% power split, the energy consumption rate at different operating conditions.

Fig. 16 The energy consumption rate at different power splits and operating conditions during the extended mission.

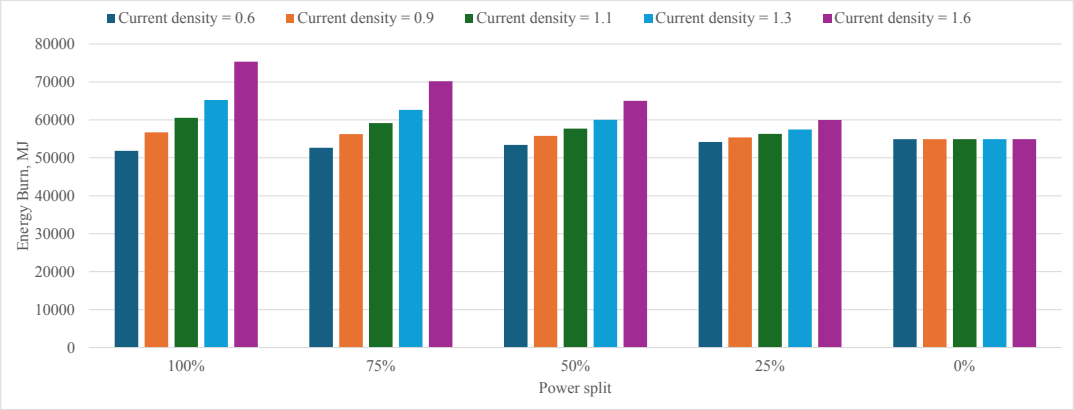

(a) The energy consumption at different current densities and power split.

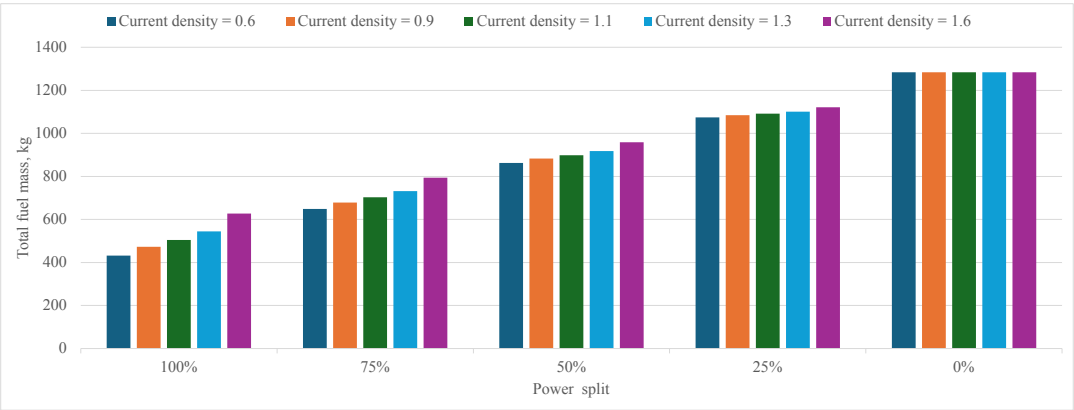

(b) The total fuel mass at different current densities and power split.

Fig. 17 The energy consumption and total fuel mass at different current densities and power split during the extended mission.

E. Passenger Seat and Payload Reduction Under Various Fuel Cell Operating Conditions

The tank size is determined by its radius and length for 100% power split, given in Table 5. The tank size remains constant regardless of the power split ratio. At a lower power split ratio, more jet fuel is carried. Since jet fuel is heavier than hydrogen, this results in a greater sacrifice of payload capacity to store the jet fuel. Therefore, for this analysis, the tank design at 100% power split is selected because it maximizes payload capability. Considering the cabin configuration of the Dash 8 Q300, including the seating map and maximum remaining payload across five cases, an estimation can be made of the passengers accommodated in the parallel hybrid turboprop aircraft. Each passenger is assumed to weigh 85 kg.

Figure 18 illustrates the situation where hydrogen tank displacement affects passenger seating. Due to the APU located in the tail of the Dash 8 Q-300, tank extension into this area is not feasible. The results in this analysis indicate that in the initial four scenarios, the increasing tank volume minimally impacts the number of passenger seats. However, in the fifth scenario, as indicated in Table 5, the tank volume increases substantially, resulting in fewer available passenger seats in spit of sufficient payload capacity to accommodate an additional passenger, as shown in Table 6. Implementing a design with higher current density extraction could further reduce available passenger seating. The passenger difference between the pre-estimated max passenger and the remaining seats is shown behind the value of the actual max passenger. Then, considering carrying only 50% of the fuel tank capacity, the analysis indicates that reducing the LH2 fuel increases the payload capability, allowing for more passengers in lower current density scenarios where additional passengers can still be accommodated. However, in higher current density scenarios such as cases 4 and 5, the passenger capacity is constrained by available seats. This limitation worsens as the payload increases. Therefore, it is better to design the fuel cell operation to avoid extreme current density conditions, whether too high or too low.

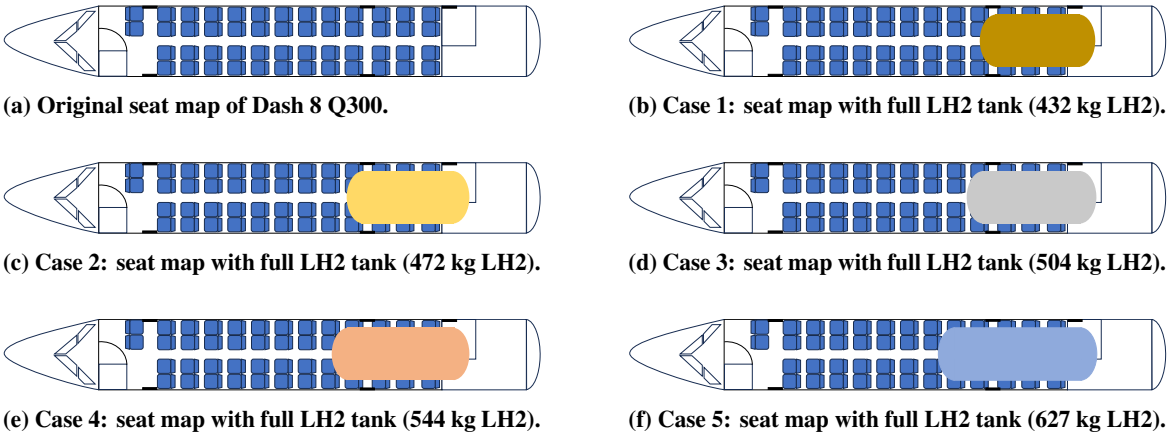

(a) Original seat map of Dash 8 Q300.

(b) Case 1: seat map with full LH2 tank (432 kg LH2).

(c) Case 2: seat map with full LH2 tank (472 kg LH2).

(d) Case 3: seat map with full LH2 tank (504 kg LH2).

(e) Case 4: seat map with full LH2 tank (544 kg LH2).

(f) Case 5: seat map with full LH2 tank (627 kg LH2).

Fig. 18 The seat reduction at different operating conditions and tank volume requirement.

Table 6 The seat reduction and actual max passengers carried at 100% power split and with 100% tank of fuel.

Item	Case 1	Case 2	Case3	Case 4	Case 5
Remaining max payload, kg	2168	2477	2553	2567	2472
Crews	2	2	2	2	2
Pre-estimated max passengers	23	27	28	28	27
Seat reduction	16	16	16	20	24
Remaining passenger seats	34	34	34	30	26
Actual max passengers	23 (-0)	27 (-0)	28 (-0)	28 (-0)	26 (-1)

Table 7 The seat reduction and actual max passengers carried at 100% power split and with 50% tank of fuel.

Item	Case 1	Case 2	Case3	Case 4	Case 5
Remaining max payload, kg	2384	2713	2805	2839	2785
Crews	2	2	2	2	2
Pre-estimated passengers	26	30	31	31	30
Seat reduction	16	16	16	20	24
Remaining passenger seats	34	34	34	30	26
Actual max passengers	26 (-0)	30 (-0)	31 (-0)	30 (-1)	26 (-4)

V. Conclusion

This research examines the correlation between system weight and volume concerning fuel cell operating conditions, hydrogen tank design, and fuel consumption. The findings reveal that the conditions yielding the minimum weight and volume are not identical. Specifically, the system achieves its minimum weight at a current density of 1.3 A/cm^2, whereas minimum volume occurs at 0.9 A/cm^2. Analysis of energy consumption indicates that higher current densities necessitate greater fuel consumption to complete missions. Furthermore, the analysis of seat reduction and actual passenger capacity shows that minimizing system weight allows for more payload capability. However, larger tanks required for minimum weight configurations can limit passenger carrying capacity. Conversely, configurations achieving the minimum system volume, while slightly heavier, still offer adequate payload capacity. Thus, this study suggests that in parallel hybrid turboprop aircraft like the Dash 8 Q300, designing and operating HT-PEMFC systems at a current density of approximately 0.9 A/cm^2 ensures energy efficiency savings and sufficient payload capacity for passenger transportation.

VI. Discussion

In practical applications, fuel cell systems typically operate at various fixed current densities and voltages. This study adopts a similar approach to model it and simulate the performance in the extended cruise mission. Based on the maximum power requirements and fuel cell performance, the number of cells installed is determined. Throughout the mission, we adjust the number of active cells according to power demand, ensuring that excess cells are not active when unnecessary, potentially sacrificing significant payload weight. Since maximum power demand occurs only shortly, dynamic control can be a possible solution to optimize payload allocation for passengers or other subsystems. The system only installs the minimum number of cells capable of meeting peak power demands through maximum power output at high current density condition. Then, during the rest of the mission, the fuel cell system can operates and shares power requirements among the minimal number of cells at lower current densities, which can work more efficiently and save more energy to complete the mission.

High-temperature proton exchange membrane fuel cells (HT-PEMFC) offer flexibility in dynamic control compared to low-temperature PEMFC (LT-PEMFC) and other fuel cell types. Unlike LT-PEMFC, which face challenges with complex water management and inlet airflow, HT-PEMFC operate without a humidifier, simplifying their dynamic management. Additionally, HT-PEMFC also shows good dynamic behaviors and faster response times compared to other fuel cell technologies. Hence, future research should explore the dynamic control capabilities of HT-PEMFC further.

This study applies open foam technology in tank design to serve as an insulation layer for maintaining liquid hydrogen temperatures. However, this approach increases tank volume. Addressing this, two methods are proposed to manage volume issues: employing multi-layer insulation (MLI) technology to reduce tank volume, and alternatively, compromising boil-off rates by reducing insulation thickness and utilizing external cooling systems for temperature maintenance. Additionally, this study does not resize tanks based on different power split ratios. Investigating these trade-offs will yield insights into optimizing LH2 tank applications in aviation.

References

[1] Darecki, M., Edelstenne, C., Enders, T., Fernandez, E., Hartman, P., Herteman, J., Kerkloh, M., King, I., Ky, P., Mathieu, M., and Orsi, G., "Flightpath 2050 : Europe's vision for aviation : maintaining global leadership and serving society's needs," Publications Office, 2011. https://doi.org/10.2777/50266.

[2] Pastra, C. L., Cinar, G., and Mavris, D. N., "Feasibility and benefit assessments of hybrid hydrogen fuel cell and battery configurations on a regional turboprop aircraft," *AIAA AVIATION 2022 Forum*, 2022, p. 3290. https://doi.org/10.2514/6.2022-3290.

[3] Troeltsch, F. M., Engelmann, M., Scholz, A. E., Peter, F., Kaiser, J., and Hornung, M., *Hydrogen Powered Long Haul Aircraft with Minimized Climate Impact*, 2020, p. 2660. https://doi.org/10.2514/6.2020-2660.

[4] Clarke, M., and Alonso, J. J., "Lithium–ion battery modeling for aerospace applications," *Journal of Aircraft*, Vol. 58, No. 6, 2021, pp. 1323–1335. https://doi.org/10.2514/1.C036209.

[5] Adler, E. J., and Martins, J. R., "Hydrogen-powered aircraft: Fundamental concepts, key technologies, and environmental impacts," *Progress in Aerospace Sciences*, Vol. 141, 2023, p. 100922. https://doi.org/10.1016/j.paerosci.2023.100922.

[6] Rendón, M. A., Sánchez R, C. D., Gallo M, J., and Anzai, A. H., "Aircraft hybrid-electric propulsion: Development trends, challenges and opportunities," *Journal of Control, Automation and Electrical Systems*, Vol. 32, No. 5, 2021, pp. 1244–1268. https://doi.org/10.1007/s40313-021-00740-x.

[7] Finger, D. F., Braun, C., and Bil, C., "Comparative assessment of parallel-hybrid-electric propulsion systems for four different aircraft," *Journal of Aircraft*, Vol. 57, No. 5, 2020, pp. 843–853. https://doi.org/10.2514/1.C035897.

[8] Onorato, G., Proesmans, P., and Hoogreef, M., "Assessment of hydrogen transport aircraft: Effects of fuel tank integration," *CEAS Aeronautical Journal*, Vol. 13, No. 4, 2022, pp. 813–845. https://doi.org/10.1007/s13272-022-00601-6.

[9] Cinar, G., Cai, Y., Bendarkar, M. V., Burrell, A. I., Denney, R. K., and Mavris, D. N., "System Analysis and Design Space Exploration of Regional Aircraft with Electrified Powertrains," *Journal of Aircraft*, Vol. 60, No. 2, 2023, p. 382–409. https://doi.org/10.2514/1.c036919.

[10] Heubner, C., Nikolowski, K., Reuber, S., Schneider, M., Wolter, M., and Michaelis, A., "Recent insights into rate performance limitations of Li-ion batteries," *Batteries & Supercaps*, Vol. 4, No. 2, 2021, pp. 268–285. https://doi.org/10.1002/batt.202000227.

[11] Gupta, S., and Perveen, R., "Fuel cell in electric vehicle," *Materials Today: Proceedings*, Vol. 79, 2023, pp. 434–437. https://doi.org/10.1016/j.matpr.2023.02.039, international Conference on Startup ventures: Technology Developments and Future Strategies.

[12] Zhang, Y., Jiang, J., An, Y., Wu, L., Dou, H., Zhang, J., Zhang, Y., Wu, S., Dong, M., Zhang, X., et al., "Sodium-ion capacitors: materials, mechanism, and challenges," *ChemSusChem*, Vol. 13, No. 10, 2020, pp. 2522–2539. https://doi.org/10.1002/cssc.201903440.

[13] De Wolf, D., and Smeers, Y., "Comparison of Battery Electric Vehicles and Fuel Cell Vehicles," *World Electric Vehicle Journal*, Vol. 14, No. 9, 2023. https://doi.org/10.3390/wevj14090262.

[14] Sousa, T., Mamlouk, M., and Scott, K., "An isothermal model of a laboratory intermediate temperature fuel cell using PBI doped phosphoric acid membranes," *Chemical Engineering Science*, Vol. 65, No. 8, 2010, pp. 2513–2530. https://doi.org/10.1016/j.ces.2009.12.038.

[15] Energy gov. (n.d.), "Hydrogen Storage," , 2020. URL https://www.energy.gov/eere/fuelcells/hydrogen-storage, last accessed December 08 2023.

[16] ZeroAvia, "Powertrain Timeline," , 2024. URL https://zeroavia.com/about-us/, last accessed January 08 2024.

[17] Universal Hydrogen, "Universal Hydrogen Successfully Completes First Flight of Hydrogen Regional Airliner," , 2023. URL https://hydrogen.aero/press-releases/universal-hydrogen-successfully-completes-first-flight-of-hydrogen-regional-airliner/, last accessed July 16 2024.

[18] Sharaf, O. Z., and Orhan, M. F., "An overview of fuel cell technology: Fundamentals and applications," *Renewable and Sustainable Energy Reviews*, Vol. 32, 2014, pp. 810–853. https://doi.org/10.1016/j.rser.2014.01.012.

[19] Hanasaki, M., Uryu, C., Daio, T., Kawabata, T., Tachikawa, Y., Lyth, S. M., Shiratori, Y., Taniguchi, S., and Sasaki, K., "SOFC durability against standby and shutdown cycling," *Journal of The Electrochemical Society*, Vol. 161, No. 9, 2014, p. F850. https://doi.org/10.1149/2.0421409jes.

[20] Kazula, S., de Graaf, S., and Enghardt, L., "Review of fuel cell technologies and evaluation of their potential and challenges for electrified propulsion systems in commercial aviation," *Journal of the Global Power and Propulsion Society*, Vol. vol. 7, 2023, pp. 43–57. URL https://elib.dlr.de/195287/.

[21] HyPoint Inc., "Hypoint's turbo air-cooled HT-PEM Fuel Cell," , 2021. URL https://docsend.com/view/t9aw2mk, last accessed January 08 2024.

[22] Sürer, M. G., and Arat, H. T., "State of art of hydrogen usage as a fuel on aviation," *European Mechanical Science*, Vol. 2, No. 1, 2018, pp. 20–30. https://doi.org/10.26701/ems.364286.

[23] Winnefeld, C., Kadyk, T., Bensmann, B., Krewer, U., and Hanke-Rauschenbach, R., "Modelling and Designing Cryogenic Hydrogen Tanks for Future Aircraft Applications," *Energies*, Vol. 11, No. 1, 2018. https://doi.org/10.3390/en11010105.

[24] International Air Transport Association (IATA) (n.d.), "Net zero roadmaps," , 2023. URL https://www.iata.org/contentassets/8d19e716636a47c184e7221c77563c93/aircraft-technology-net-zero-roadmap.pdf, last accessed December 09 2023.

[25] Mirjalili, S., and Lewis, A., "The Whale Optimization Algorithm," *Advances in Engineering Software*, Vol. 95, 2016, pp. 51–67. https://doi.org/10.1016/j.advengsoft.2016.01.008.

[26] Li, Y., Han, T., Zhao, H., and Gao, H., "An adaptive whale optimization algorithm using Gaussian distribution strategies and its application in heterogeneous UCAVs task allocation," *IEEE Access*, Vol. 7, 2019, pp. 110138–110158. https://doi.org/10.1109/ACCESS.2019.2933661.

[27] Prewitz, M., Schwärzer, J., and Bardenhagen, A., "Potential analysis of hydrogen storage systems in aircraft design," *International Journal of Hydrogen Energy*, Vol. 48, No. 65, 2023, pp. 25538–25548. https://doi.org/10.1016/j.ijhydene.2023.03.266.

[28] Ahluwalia, R., Roh, H.-S., Peng, J.-K., Papadias, D., Baird, A., Hecht, E., Ehrhart, B., Muna, A., Ronevich, J., Houchins, C., Killingsworth, N., and Aceves, S., "Liquid hydrogen storage system for heavy duty trucks: Configuration, performance, cost, and safety," *International Journal of Hydrogen Energy*, Vol. 48, No. 35, 2023, pp. 13308–13323. https://doi.org/10.1016/j.ijhydene.2022.12.152.

[29] Rosli, R., Sulong, A., Daud, W., Zulkifley, M., Husaini, T., Rosli, M., Majlan, E., and Haque, M., "A review of high-temperature proton exchange membrane fuel cell (HT-PEMFC) system," *International Journal of Hydrogen Energy*, Vol. 42, No. 14, 2017, pp. 9293–9314. https://doi.org/10.1016/j.ijhydene.2016.06.211.

[30] Scott, K., Pilditch, S., and Mamlouk, M., "Modelling and experimental validation of a high temperature polymer electrolyte fuel cell," *Journal of Applied Electrochemistry*, Vol. 37, 2007, pp. 1245–1259. https://doi.org/10.1007/s10800-007-9414-1.

[31] Cheddie, D., and Munroe, N., "Mathematical model of a PEMFC using a PBI membrane," *Energy Conversion and Management*, Vol. 47, No. 11, 2006, pp. 1490–1504. https://doi.org/10.1016/j.enconman.2005.08.002.

[32] Bayat, M., and Özalp, M., "Effects of leak current density and doping level on energetic, exergetic and ecological performance of a high-temperature PEM fuel cell," *International Journal of Hydrogen Energy*, Vol. 48, No. 60, 2023, pp. 23212–23229. https://doi.org/10.1016/j.ijhydene.2023.03.277.

[33] Li, Q., Aili, D., Hjuler, H. A., and Jensen, J. O., "High temperature polymer electrolyte membrane fuel cells," *Cham Heidelberg New York Dordrecht London: Springer*, 2016, p. 545. URL https://link.springer.com/content/pdf/10.1007/978-3-319-17082-4.pdf.

[34] Olapade, P. O., Meyers, J. P., Borup, R. L., and Mukundan, R., "Parametric study of the morphological proprieties of HT-PEMFC components for effective membrane hydration," *Journal of The Electrochemical Society*, Vol. 158, No. 6, 2011, p. B639. https://doi.org/10.1149/1.3569711.

[35] Ma, Y.-L., Wainright, J., Litt, M., and Savinell, R., "Conductivity of PBI membranes for high-temperature polymer electrolyte fuel cells," *Journal of the Electrochemical Society*, Vol. 151, No. 1, 2003, p. A8. https://doi.org/10.1149/1.1630037.

[36] Jiao, K., and Li, X., "A Three-Dimensional Non-isothermal Model of High Temperature Proton Exchange Membrane Fuel Cells with Phosphoric Acid Doped Polybenzimidazole Membranes," *Fuel Cells*, Vol. 10, No. 3, 2010, pp. 351–362. https://doi.org/10.1002/fuce.200900059.

[37] Zhang, C., Liu, Z., Zhou, W., Chan, S. H., and Wang, Y., "Dynamic performance of a high-temperature PEM fuel cell – An experimental study," *Energy*, Vol. 90, 2015, pp. 1949–1955. https://doi.org/https://doi.org/10.1016/j.energy.2015.07.026, URL https://www.sciencedirect.com/science/article/pii/S0360544215009214.

[38] Guo, X., Guo, Y., Wang, J., Xiao, B., Cao, Y., and Wu, C., "Thermodynamic analysis and optimization of a novel hybrid system using thermoacoustic cycle to harvest waste heat of high temperature PEMFC," *Energy Conversion and Management*, Vol. 260, 2022, p. 115572. https://doi.org/10.1016/j.enconman.2022.115572.

[39] FlightAware, "de Havilland Dash 8-300," , 2023. URL https://www.flightaware.com/, last accessed December 08 2023.

[40] Air Inuit, "De Havilland Dash-8 Combi 300," , 2023. URL https://www.airinuit.com/en/charter/fleet/de-havilland-dash-8-combi-300, last accessed November 12 2023.

[41] Aircraft Commerce, "Dash 8 & Q Series specifications," , 2009. URL https://www.aircraft-commerce.com/wp-content/uploads/aircraft-commerce-docs/Aircraft%20guides/DASH%208%20&%20Q%20SERIES/ISSUE63_DASH8SPECS.pdf, last accessed November 12 2023.

[42] Airlines Inform, "Bombardier Dash 8 Q300," , 2008. URL https://www.airlines-inform.com/commercial-aircraft/dash-8q300.html, last accessed November 12 2023.

[43] Sforza, P. M., "Direct calculation of zero-lift drag coefficients and (L/D) max in subsonic cruise," *Journal of aircraft*, Vol. 57, No. 6, 2020, pp. 1224–1228. https://doi.org/10.2514/1.C035717.

[44] Cinar, G., "A methodology for dynamic sizing of electric power generation and distribution architectures," 2018. https://doi.org/http://hdl.handle.net/1853/60754.

[45] Cinar, G., "A methodology for dynamic sizing of electric power generation and distribution architectures," 2018.

[46] Cinar, G., Garcia, E., and Mavris, D. N., "A framework for Electrified Propulsion Architecture and Operation Analysis," *Aircraft Engineering and Aerospace Technology*, Vol. 92, No. 5, 2020, pp. 675–684. https://doi.org/10.1108/AEAT-06-2019-0118.

[47] López, I., Ibarra, E., Matallana, A., Andreu, J., and Kortabarria, I., "Next generation electric drives for HEV/EV propulsion systems: Technology, trends and challenges," *Renewable and Sustainable Energy Reviews*, Vol. 114, 2019, p. 109336. https://doi.org/https://doi.org/10.1016/j.rser.2019.109336, URL https://www.sciencedirect.com/science/article/pii/S1364032119305441.

[48] Spakovszky, Z. S., Chen, Y., Greitzer, E. M., Cordero, Z. C., Lang, J. H., Kirtley, J. L., Perreault, D. J., Andersen, H. N., Qasim, M. M., Cuadrado, D. G., et al., "A Megawatt-Class Electrical Machine Technology Demonstrator For Turbo-Electric Propulsion," *AIAA AVIATION 2023 Forum*, 2023, p. 4157. https://doi.org/10.2514/6.2023-4157.

[49] Schmelcher, M., and Häßy, J., "Hydrogen fuel cells for aviation? A potential analysis comparing different thrust categories," 2022. URL https://elib.dlr.de/188835/, last accessed January 13 2024.

[50] Brewer, G. D., *Hydrogen aircraft technology*, Routledge, 2017. https://doi.org/10.1201/9780203751480.

[51] Devrim, Y., Albostan, A., and Devrim, H., "Experimental investigation of CO tolerance in high temperature PEM fuel cells," *International Journal of Hydrogen Energy*, Vol. 43, No. 40, 2018, pp. 18672–18681. https://doi.org/10.1016/j.ijhydene.2018.05.085.

[52] Shamardina, O., Chertovich, A., Kulikovsky, A., and Khokhlov, A., "A simple model of a high temperature PEM fuel cell," *International Journal of Hydrogen Energy*, Vol. 35, No. 18, 2010, pp. 9954–9962. https://doi.org/10.1016/j.ijhydene.2009.11.012.

[53] Hoeflinger, J., and Hofmann, P., "Air mass flow and pressure optimisation of a PEM fuel cell range extender system," *international journal of hydrogen energy*, Vol. 45, No. 53, 2020, pp. 29246–29258. https://doi.org/https://doi.org/10.1016/j.ijhydene.2020.07.176.

[54] Díaz, M. A., Iranzo, A., Rosa, F., Isorna, F., López, E., and Bolivar, J. P., "Effect of carbon dioxide on the contamination of low temperature and high temperature PEM (polymer electrolyte membrane) fuel cells. Influence of temperature, relative humidity and analysis of regeneration processes," *Energy*, Vol. 90, 2015, pp. 299–309. https://doi.org/https://doi.org/10.1016/j.energy.2015.06.097, URL https://www.sciencedirect.com/science/article/pii/S0360544215008531.

[55] Xia, L., Zhang, C., Hu, M., Jiang, S., Chin, C. S., Gao, Z., and Liao, Q., "Investigation of parameter effects on the performance of high-temperature PEM fuel cell," *International Journal of Hydrogen Energy*, Vol. 43, No. 52, 2018, pp. 23441–23449. https://doi.org/https://doi.org/10.1016/j.ijhydene.2018.10.210, URL https://www.sciencedirect.com/science/article/pii/S0360319918334736.